The Astrophysical Journal, 907:78 (24pp), 2021 February 1 https://doi.org/10.3847/1538-4357/abcaf6

Afterglow Light Curves of Nonrelativistic Ejecta Mass in a Stratified Circumstellar Medium

N. Fraija[1], B. Betancourt Kamenetskaia[1,2,3], M. G. Dainotti[4,5,6,7], R. Barniol Duran[8], A. Gálvan Gámez[1], S. Dichiara[9,10], and A. C. Caligula do E. S. Pedreira[1]

[1] Instituto de Astronomía, Universidad Nacional Autónoma de México, Circuito Exterior, C.U., A. Postal 70-264, 04510 México City, México
nifraija@astro.unam.mx
[2] LMU Physics Department, Ludwig Maximilians University, Theresienstr. 37, D-80333 Munich, Germany
[3] TUM Physics Department, Technical University of Munich, James-Franck-Str., D-85748 Garching, Germany
[4] Physics Department, Stanford University, 382 Via Pueblo Mall, Stanford, USA
[5] Space Science Institute, Boulder, CO, USA
[6] Obserwatorium Astronomiczne, Uniwersytet Jagielloński, ul. Orla 171, 31-501 Kraków, Poland
[7] Interdisciplinary Theoretical & Mathematical Science Program, RIKEN (iTHEMS), 2-1 Hirosawa, Wako, Saitama, 351-0198, Japan
[8] Department of Physics and Astronomy, California State University, Sacramento, 6000 J Street, Sacramento, CA 95819-6041, USA
[9] Department of Astronomy, University of Maryland, College Park, MD 20742-4111, USA
[10] Astrophysics Science Division, NASA Goddard Space Flight Center, 8800 Greenbelt Road, Greenbelt, MD 20771, USA
Received 2020 July 13; revised 2020 October 22; accepted 2020 November 14; published 2021 February 1

Abstract

We present the afterglow light curves produced by the deceleration of a nonrelativistic ejecta mass in a stratified circumstellar medium with a density profile $n(r) \propto r^{-k}$ with $k = 0$, 1, 1.5, 2, and 2.5. Once the ejecta mass is launched with equivalent kinetic energy parameterized by $E(>\beta) \propto \beta^{-\alpha}$ (where β is the ejecta velocity) and propagates into the surrounding circumstellar medium, it first moves with constant velocity (the free-coasting phase), and later it decelerates (the Sedov–Taylor expansion). We present the predicted synchrotron and synchrotron self-Compton light curves during the free-coasting phase and the subsequent Sedov–Taylor expansion. In particular cases, we show the corresponding light curves generated by the deceleration of several ejecta masses with different velocities launched during the coalescence of binary compact objects and the core collapse of dying massive stars, which will contribute at distinct timescales, frequencies, and intensities. Finally, using the multiwavelength observations and upper limits collected by a large campaign of orbiting satellites and ground telescopes, we constrain the parameter space of both the kilonova (KN) afterglow in GW170817 and the possibly generated KN afterglow in S190814bv. Further observations on timescales of years post-merger are needed to derive tighter constraints.

Unified Astronomy Thesaurus concepts: Gamma-ray bursts (629); Gravitational wave astronomy (675); Non-thermal radiation sources (1119); Compact binary stars (283)

1. Introduction

Long-duration gamma-ray bursts (lGRBs; $T_{90} \gtrsim 2$ s; Kouveliotou et al. 1993) are connected with the core collapse (CC) of dying massive stars (Woosley 1993; Galama et al. 1998), which leads to supernovae (SNe; Bloom et al. 1999; Woosley & Bloom 2006). Short-duration gamma-ray bursts (sGRBs; $T_{90} \lesssim 2$ s) are associated with the coalescence of binary compact objects (NS–NS or BH–NS),[11] which leads to kilonovae[12] (KNe; Li & Paczyński 1998; Rosswog 2005; Metzger et al. 2010; Kasen et al. 2013; Metzger 2017). The death of massive stars and the coalescence of binary compact objects are believed to launch considerable amounts of materials with broad ranges of velocities. In the framework of NS–NS mergers, nonrelativistic ejecta masses with velocities in the range $0.03 \lesssim \beta \lesssim 0.8$ (expressed hereafter in units of the speed of light), such as dynamical ejecta, cocoon material, shock breakout material, and wind ejecta, are launched (e.g., see Dessart et al. 2009; Goriely et al. 2011; Bauswein et al. 2013; Hotokezaka et al. 2013; Kyutoku et al. 2014; Metzger & Fernández 2014; Murguia-Berthier et al. 2014; Nagakura et al. 2014; Wanajo et al. 2014; Fernández et al. 2015; Metzger et al. 2015; Lazzati et al. 2017, 2018). In the framework of CC-SNe (depending on the type of SN association), several ejecta masses with nonrelativistic velocities of $\beta \lesssim 0.3$ have been reported (e.g., see Kulkarni et al. 1998; Bloom et al. 1999; Woosley & Bloom 2006; Valenti et al. 2008; Gal-Yam 2017; Izzo et al. 2019, 2020; Modjaz et al. 2020; Nicholl et al. 2020). While the inferred mass of the ejecta for the first gamma-ray burst (GRB)/SN association (GRB 980425/SN 1998bw; Kulkarni et al. 1998) was $10^{-5}\,M_{\odot}$ with a velocity of $\beta \sim 0.2$–0.3, the inferred mass for the first GRB/KN association (GRB 170817A/AT 2017gfo; Coulter et al. 2017) was 10^{-4}–$10^{-2}\,M_{\odot}$, ejected with a velocity of $\beta \sim 0.1$–0.3 (Arcavi et al. 2017; Cowperthwaite et al. 2017; Nicholl et al. 2017; Metzger 2019). Chevalier (1982) studied the interaction of an adiabatic flow in a circumstellar density profile for SNe II of the form $n(r) \propto r^{-2}$. Such a power law (PL) has since been the usual convention, and it has been used in subsequent papers for different types of SNe, such as those by Kotak et al. (2004), Chevalier (1984), Soderberg et al. (2006), and Blondin et al. (1996). However, in a more recent study, Moriya & Tominaga (2012) showed that the spectral diversity of Type II luminous SNe may be explained by the diversity in the density slope of the surrounding dense wind. Accordingly, they proposed a wind density structure with a profile of $\propto r^{-k}$ and noticed that the ratio of the diffusion timescale in the optically thick region of the wind to the shock propagation timescale after shock

[11] NS corresponds to neutron star and BH to black hole.
[12] A fairly isotropic thermal transient powered by the radioactive decay of rapid neutron capture process nuclei and isotopes.

breakout had a strong dependence on the stratification parameter k, which led to differences in the SN spectral evolution.

The interaction of the ejecta mass with the surrounding circumburst medium in the nonrelativistic regime has been proposed for use in describing multiwavelength afterglow observations in timescales of days to several years (e.g., see Wijers et al. 1997; Dai & Lu 1999; Huang et al. 1999; Livio & Waxman 2000; Huang & Cheng 2003; Sironi & Giannios 2013; Barniol Duran & Giannios 2015). Several authors (e.g., Metzger & Bower 2014; Fong et al. 2016; Liu et al. 2020; Schroeder et al. 2020) have considered the material launched during the coalescence of binary compact objects and computed the synchrotron emission in the radio bands. These authors have assumed a free-coasting phase and a subsequent Sedov–Taylor expansion. Tan et al. (2001) considered that the kinetic energy of the shock wave could be described in terms of a PL velocity distribution. Thenceforth, several authors have considered that the material launched during the coalescence of binary compact objects and CC-SNe may be described by a PL velocity distribution (e.g., Lazzati et al. 2012; Bauswein et al. 2013; Horesh et al. 2013; Margutti et al. 2013, 2014; Kyutoku et al. 2014; Barniol Duran et al. 2015; Hotokezaka & Piran 2015; Metzger 2017, 2019; Mooley et al. 2018b; Fraija et al. 2019d; Kathirgamaraju et al. 2019). In the context of the coalescence of an NS binary, Fraija et al. (2019d) and Kathirgamaraju et al. (2019), for instance, assumed a PL distribution for the energy of the shock breakout (the outermost matter) and the KN material in GW170817 and calculated the nonthermal emission generated by the interaction of these materials with the uniform-density medium. In the case of dying massive stars, Lazzati et al. (2012), for example, presented a set of numerical simulations of stellar explosions induced by outflows and compared the results with observational properties of SNe Ibc as a function of the equivalent kinetic energy and velocity of the ejecta.

In this paper, we present, based on analytic arguments, a theoretical model that predicts the multiwavelength afterglow emission generated by the deceleration of a nonrelativistic ejecta mass in a circumstellar medium with a profile of $n(r) \propto r^{-k}$. Once the ejecta mass propagates into the circumstellar medium, it first moves with a constant velocity, and later, when the swept-up quantity of material is similar to the ejected mass, it begins to decelerate. During these stages, electrons are accelerated in the forward shocks and are cooled down by synchrotron and synchrotron self-Compton (SSC) processes. We present the predicted synchrotron and SSC light curves for $k = 0$, 1, 1.5, 2, and 2.5 that cover several ejecta masses launched during the coalescence of binary compact objects and CC-SNe. In particular, with multiwavelength observations and upper limits collected by a large campaign of orbiting satellites and ground telescopes, we constrain the parameter space of both the KN afterglow in GW170817 and the possibly generated KN afterglow produced by the coalescence of a BH–NS system in S190814bv. The paper is organized as follows: In Section 2, we introduce the theoretical model that predicts the multiwavelength afterglow emission generated by the deceleration of a nonrelativistic ejecta mass. In Section 3, we show the predicted synchrotron and SSC light curves for a density profile with $k = 0$, 1, 1.5, 2, and 2.5. In Section 4, we show the synchrotron and SSC light curves from material launched during the coalescence of an NS binary. In Section 5, we discuss the nonrelativistic ejected mass around the KN emission. In Section 6, we apply our model to two particular cases, to GW170817 and S190814bv, and finally in Section 7, we present a discussion and summary. We adopt the convention $Q_x = \frac{Q}{10^x}$ in cgs units and assume for the cosmological constants a spatially flat universe ΛCDM model with $H_0 = 69.6\,\mathrm{km\,s^{-1}\,Mpc^{-1}}$, $\Omega_{\rm M} = 0.286$, and $\Omega_\Lambda = 0.714$ (Planck Collaboration et al. 2016). Primed and unprimed quantities are used for the comoving and observer frames, respectively.

2. Afterglow Light Curves of a Nonrelativistic Ejecta Mass

In this section, we show the dynamics of the forward shocks given by the deceleration of the ejecta mass in a density profile $n(r) = A_k r^{-k}$ with A_k denoting the density parameter and $0 \leqslant k < 3$. We use analytical arguments in order to compute the synchrotron and SSC light curves expected in the nonrelativistic regime. The synchrotron and SSC radiation is derived in the fully adiabatic regime during the free-coasting and deceleration phases assuming an electron distribution described by $dN/d\gamma_{\rm e} \propto \gamma_{\rm e}^{-p}$, for $\gamma_{\rm e} \geqslant \gamma_{\rm m}$, where $\gamma_{\rm m}$ is the Lorentz factor of the lowest-energy electrons and p is the index of the electron distribution. We only consider the dynamics of the forward shocks instead of including that of reverse shocks because electrons accelerated in reverse shocks generate short-lived emissions and we are interested in describing emissions extended in timescales of days to years.

Irrespective of the progenitor, nonrelativistic materials with a wide range of masses and velocities are launched into the circumstellar medium. After a time t following the coalescence or collapse, a generic ejecta mass moves with a constant velocity β and expands with a mean radius $r \approx \beta t$ (e.g., see Kulkarni et al. 1998; Metzger 2019). The initial expansion phase is not affected by the circumstellar medium, but once the swept-up quantity of material is as large as the ejected mass, the ejecta begins to decelerate (Rosswog et al. 2014). During the deceleration phase, numerical simulations indicate that the velocity of matter in front of the ejecta is higher than that of matter moving in the back, so that the ejecta acquires a velocity structure (e.g., see Tan et al. 2001; Rosswog et al. 2014).

2.1. The Free-coasting Phase

During the initial expansion, the ejecta mass is not affected by the circumstellar medium (Rosswog et al. 2014), so the velocity is constant $\beta \propto t^0$ and the radius evolves as $r \propto (1+z)^{-1} t$.

2.1.1. Synchrotron Emission

During the coasting phase, the post-shock magnetic field evolves as $B' \propto \epsilon_B^{\frac{1}{2}} A_k^{\frac{1}{2}} \beta^{\frac{2-k}{2}} t^{-\frac{k}{2}}$, where ϵ_B is a microphysical parameter associated with the magnetic density. The Lorentz factors of the lowest-energy electrons and of the higher-energy electrons, which are efficiently cooled by synchrotron emission, are

$$\gamma_{\rm m} = \gamma_{\rm m}^0\, g(p)\, \epsilon_{\rm e,-1}\, \beta_{-0.5}^2$$
$$\gamma_{\rm c} = \gamma_{\rm c}^0 \left(\frac{1+z}{1.022}\right)^{1-k} (1+Y)^{-1}\, \epsilon_{B,-2}^{-1}\, A_k^{-1} \beta_{-0.5}^{k-2}\, t_6^{k-1}, \qquad (1)$$

where Y is the Compton parameter (Sari & Esin 2001), $g(p) = \frac{p-2}{p-1}$, $\epsilon_{\rm e}$ is a microphysical parameter associated with

the electron density, and z is the redshift of a generic observer located at 100 Mpc. Given the evolution of the synchrotron frequencies as a function of the electron Lorentz factors $\nu_i^{\rm syn} \propto \gamma_i^2$ with $i = {\rm m}$ or c, using Equation (1) the corresponding synchrotron break frequencies can be written as

$$\nu_{\rm m}^{\rm syn} = \nu_{\rm m}^{\rm syn,0}\, g^2(p) \left(\frac{1+z}{1.022}\right)^{\frac{k-2}{2}} \epsilon_{\rm e,-1}^2\, \epsilon_{B,-1}^{\frac{1}{2}} A_k^{\frac{1}{2}} \beta_{-0.5}^{\frac{10-k}{2}}\, t_6^{-\frac{k}{2}}$$
$$\nu_{\rm c}^{\rm syn} = \nu_{\rm c}^{\rm syn,0} \left(\frac{1+z}{1.022}\right)^{\frac{2-3k}{2}} (1+Y)^{-2}\, \epsilon_{B,-2}^{-\frac{3}{2}} A_k^{-\frac{3}{2}} \beta_{-0.5}^{\frac{3k-6}{2}}\, t_6^{\frac{3k-4}{2}}. \quad (2)$$

In the self-absorption regime, the synchrotron break frequencies are (Panaitescu & Kumar 2000; Gao et al. 2015)

$$\nu_{\rm a,1}^{\rm syn} = \nu_{\rm a,1}^{\rm syn,0} \left(\frac{1+z}{1.022}\right)^{\frac{4(k-2)}{5}} g(p)^{-1}\, \epsilon_{\rm e,-1}^{-1}\, \epsilon_{B,-2}^{\frac{1}{5}} A_k^{\frac{4}{5}} \beta_{-0.5}^{-\frac{4k+5}{5}}\, t_6^{\frac{3-4k}{5}},$$
$$\nu_{\rm a,2}^{\rm syn} = \nu_{\rm a,2}^{\rm syn,0} \left(\frac{1+z}{1.022}\right)^{\frac{(k-2)(p+6)}{2(p+4)}} g(p)^{\frac{2(p-1)}{p+4}}\, \epsilon_{\rm e,-1}^{\frac{2(p-1)}{p+4}}\, \epsilon_{B,-2}^{\frac{p+2}{2(p+4)}}$$
$$\times A_k^{\frac{p+6}{2(p+4)}} \beta_{-0.5}^{\frac{10p-kp-6k}{2(p+4)}}\, t_6^{\frac{4-kp-6k}{2(p+4)}},$$
$$\nu_{\rm a,3}^{\rm syn} = \nu_{\rm a,3}^{\rm syn,0} \left(\frac{1+z}{1.022}\right)^{\frac{9k-13}{5}} (1+Y)\, \epsilon_{B,-2}^{\frac{6}{5}} A_k^{\frac{9}{5}} \beta_{-0.5}^{\frac{15-9k}{5}}\, t_6^{\frac{8-9k}{5}}, \quad (3)$$

where $\nu_{{\rm a},l}^{\rm syn}$ for $l = 1$, 2, and 3 are defined in the ranges $\nu_{\rm a,1}^{\rm syn} \leqslant \nu_{\rm m}^{\rm syn} \leqslant \nu_{\rm c}^{\rm syn}$, $\nu_{\rm m}^{\rm syn} \leqslant \nu_{\rm a,2}^{\rm syn} \leqslant \nu_{\rm c}^{\rm syn}$, and $\nu_{\rm a,3}^{\rm syn} \leqslant \nu_{\rm c}^{\rm syn} \leqslant \nu_{\rm m}^{\rm syn}$, respectively. Taking into account that the peak spectral power evolves as $P_{\nu,\max} \propto (1+z)^{\frac{k-2}{2}}\, \epsilon_B^{\frac{1}{2}} A_k^{\frac{1}{2}}\, \beta^{\frac{2-k}{2}}\, t^{-\frac{k}{2}}$ and that the number of swept-up electrons in the post-shock is $N_{\rm e} \propto (1+z)^{k-3} A_k \beta^{3-k} t^{3-k}$, the spectral peak flux density is given by

$$F_{\nu,\max}^{\rm syn} = F_{\nu,\max}^{\rm syn,0} \left(\frac{1+z}{1.022}\right)^{\frac{3k-4}{2}} \epsilon_{B,-2}^{\frac{1}{2}}\, d_{z,26.5}^{-2}\, A_k^{\frac{3}{2}}\, \beta_{-0.5}^{\frac{8-3k}{2}}\, t_6^{\frac{3(2-k)}{2}}, \quad (4)$$

where $d_z = (1+z)\frac{c}{H_0}\int_0^z \frac{d\tilde{z}}{\sqrt{\Omega_{\rm M}(1+\tilde{z})^3+\Omega_\Lambda}}$ (Weinberg 1972) is the luminosity distance with c denoting the speed of light. The terms $\gamma_{\rm m}^0$, $\gamma_{\rm c}^0$, $\nu_{\rm m}^{\rm syn,0}$, $\nu_{\rm c}^{\rm syn,0}$, and $F_{\nu,\max}^{\rm syn,0}$ are given in Table 1 for $k = 0$, 1, 1.5, 2, and 2.5.

Using the synchrotron break frequencies (Equations (2) and (3)) and the spectral peak flux density (Equation (4)), the synchrotron light curves in the fast- and slow-cooling regimes evolve as

$$F_\nu^{\rm syn} \propto \begin{cases} t^{1+k}\, \nu^2, & \nu < \nu_{\rm a,3}^{\rm syn}, \\ t^{\frac{11-6k}{3}}\, \nu^{\frac{1}{3}}, & \nu_{\rm a,3}^{\rm syn} < \nu < \nu_{\rm c}^{\rm syn}, \\ t^{\frac{8-3k}{4}}\, \nu^{-\frac{1}{2}}, & \nu_{\rm c}^{\rm syn} < \nu < \nu_{\rm m}^{\rm syn}, \\ t^{\frac{8-k(p+2)}{4}}\, \nu^{-\frac{p}{2}}, & \nu_{\rm m}^{\rm syn} < \nu, \end{cases} \quad (5)$$

$$F_\nu^{\rm syn} \propto \begin{cases} t^2\, \nu^2, & \nu < \nu_{\rm a,1}^{\rm syn}, \\ t^{\frac{9-4k}{3}}\, \nu^{\frac{1}{3}}, & \nu_{\rm a,1}^{\rm syn} < \nu < \nu_{\rm m}^{\rm syn}, \\ t^{\frac{12-k(p+5)}{4}}\, \nu^{-\frac{p-1}{2}}, & \nu_{\rm m}^{\rm syn} < \nu < \nu_{\rm c}^{\rm syn}, \\ t^{\frac{8-k(p+2)}{4}}\, \nu^{-\frac{p}{2}}, & \nu_{\rm c}^{\rm syn} < \nu, \end{cases} \quad (6)$$

and

$$F_\nu^{\rm syn} \propto \begin{cases} t^2\, \nu^2, & \nu < \nu_{\rm m}^{\rm syn}, \\ t^{\frac{8+k}{4}}\, \nu^{\frac{5}{2}}, & \nu_{\rm m}^{\rm syn} < \nu < \nu_{\rm a,2}^{\rm syn}, \\ t^{\frac{12-k(p+5)}{4}}\, \nu^{-\frac{p-1}{2}}, & \nu_{\rm a,2}^{\rm syn} < \nu < \nu_{\rm c}^{\rm syn}, \\ t^{\frac{8-k(p+2)}{4}}\, \nu^{-\frac{p}{2}}, & \nu_{\rm c}^{\rm syn} < \nu, \end{cases} \quad (7)$$

respectively. It is worth noting that the synchrotron light curves in the fast-cooling regime are derived for completeness, since they are not relevant for the problems investigated here.

2.1.2. SSC Emission

The electron distribution accelerated during the forward shock upscatters synchrotron photons, yielding the SSC spectrum, which is characterized by break frequencies $\nu_{ij}^{\rm ssc} = 4\gamma_i^2 \nu_j^{\rm syn} x_0$ with i, $j = {\rm a}$, m, or c and x_0 denoting a parameter that ensures energy conservation (e.g., see Sari & Esin 2001; Zhang & Mészáros 2001; Gao et al. 2013b). The SSC break frequencies, the corresponding spectral peak flux density, and the light curves in the fast- and slow-cooling regimes are shown in the Appendix.

2.2. The Deceleration Phase

During the deceleration phase, the ejecta acquires a velocity structure: the velocity of matter in front of the ejecta is higher than that of matter moving in the back (Sari & Mészáros 2000). Tan et al. (2001) studied the acceleration of the ejecta mass with relativistic and subrelativistic velocities. They found that the equivalent kinetic energy in the non- and ultrarelativistic limits can be expressed as a PL velocity distribution given by $E_k\ (\geqslant\beta) \propto \beta^{-5.2}$ for $\beta \ll 1$ and $E_k(\geqslant\beta\Gamma) \propto (\beta\Gamma)^{-1.1}$ for $\beta\Gamma \gg 1$ (with $\Gamma = \sqrt{1/1-\beta^2}$), respectively.[13] Here, we consider the nonrelativistic regime, so the equivalent kinetic energy distribution given by $E_k(\geqslant\beta) = \tilde{E}\ \beta^{-\alpha}$ with $\tilde{E}$ denoting the fiducial energy and $3 \leqslant \alpha \leqslant 5.2$ is used. We adopt this range of values motivated by the numerical simulations presented in Tan et al. (2001).

During this phase the dynamics of the nonrelativistic ejecta mass is described by the Sedov–Taylor solution. Then, the velocity and the blast wave radius can be written as

$$\beta = \beta^0 \left(\frac{1+z}{1.022}\right)^{\frac{3-k}{\alpha+5-k}} A_k^{-\frac{1}{\alpha+5-k}}\, \tilde{E}_{51}^{\frac{1}{\alpha+5-k}}\, t_7^{\frac{k-3}{\alpha+5-k}}, \quad (8)$$

and

$$r = r^0 \left(\frac{1+z}{1.022}\right)^{-\frac{\alpha+2}{\alpha+5-k}} A_k^{-\frac{1}{\alpha+5-k}}\, \tilde{E}_{51}^{\frac{1}{\alpha+5-k}}\, t_7^{\frac{\alpha+2}{\alpha+5-k}}, \quad (9)$$

respectively, where the fiducial energy ($\tilde{E}$) can be estimated by calculating the term $\propto\beta^2 r^3$. From Equation (8) it can be noted that the deceleration time evolves as

$$t_{\rm dec} = t_{\rm dec}^0 \left(\frac{1+z}{1.022}\right) A_k^{\frac{1}{k-3}}\, \tilde{E}_{51}^{\frac{1}{3-k}}\, \beta_{-0.5}^{\frac{\alpha+5-k}{k-3}}. \quad (10)$$

The terms r^0 and $t_{\rm dec}^0$ are given in Table 1 for $k = 0$, 1, 1.5, 2, and 2.5. It is worth noting that for a uniform-density medium

[13] A polytropic index $n_{\rm p} = 3$ is used.

($k = 0$) and $\alpha = 0$, the velocity and blast wave radius derived in Sironi & Giannios (2013) are recovered.

2.2.1. Synchrotron Emission

During the deceleration phase, the post-shock magnetic field evolves as $B' \propto t^{-\frac{6+k\alpha}{2(\alpha+5-k)}}$. The Lorentz factors of the lowest-energy electrons and of the higher-energy electrons, which are efficiently cooled by synchrotron emission, are

$$\gamma_{\rm m} = \gamma_{\rm m}^0 \left(\frac{1+z}{1.022}\right)^{\frac{2(3-k)}{\alpha+5-k}} g(p)\,\epsilon_{\rm e,-1}\,A_k^{-\frac{2}{\alpha+5-k}}\,\tilde{E}_{51}^{\frac{2}{\alpha+5-k}}\,t_7^{\frac{2(k-3)}{\alpha+5-k}}$$
$$\gamma_{\rm c} = \gamma_{\rm c}^0 \left(\frac{1+z}{1.022}\right)^{-\frac{k+1+\alpha(k-1)}{\alpha+5-k}} (1+Y)^{-1}\epsilon_{B,-2}^{-1}\,A_k^{-\frac{\alpha+3}{\alpha+5-k}} \times \tilde{E}_{51}^{\frac{k-2}{\alpha+5-k}}\,t_7^{\frac{k+1+\alpha(k-1)}{\alpha+5-k}}. \quad (11)$$

The corresponding synchrotron break frequencies are given by

$$\nu_{\rm m}^{\rm syn} = \nu_{\rm m}^{\rm syn,0}\left(\frac{1+z}{1.022}\right)^{\frac{20+k(\alpha-6)-2\alpha}{2(\alpha+5-k)}} g(p)^2\epsilon_{\rm e,-1}^2\,\epsilon_{B,-2}^{\frac{1}{2}}\,A_k^{\frac{\alpha-5}{2(\alpha+5-k)}} \times \tilde{E}_{51}^{\frac{10-k}{2(\alpha+5-k)}}\,t_7^{-\frac{30+k(\alpha-8)}{2(\alpha+5-k)}}$$
$$\nu_{\rm c}^{\rm syn} = \nu_{\rm c}^{\rm syn,0}\left(\frac{1+z}{1.022}\right)^{-\frac{8-2\alpha+k(3\alpha+2)}{2(\alpha+5-k)}} \epsilon_{B,-2}^{-\frac{3}{2}}\,(1+Y)^{-2} \times A_k^{-\frac{3(\alpha+3)}{2(\alpha+5-k)}}\tilde{E}_{51}^{\frac{3(k-2)}{2(\alpha+5-k)}}\,t_7^{\frac{k(4+3\alpha)-4\alpha-2}{2(\alpha+5-k)}}. \quad (12)$$

In the self-absorption regime, the synchrotron break frequencies are

$$\nu_{\rm a,1}^{\rm syn} = \nu_{\rm a,1}^{\rm syn,0}\left(\frac{1+z}{1.022}\right)^{m_{11}} g(p)^{-1}\epsilon_{\rm e,-1}^{-1}\epsilon_{B,-2}^{\frac{1}{5}}\,A_k^{\frac{25+4\alpha}{5(\alpha+5-k)}} \times \tilde{E}_{51}^{-\frac{4k+5}{5(\alpha+5-k)}}t_6^{m_{21}}$$
$$\nu_{\rm a,2}^{\rm syn} = \nu_{\rm a,2}^{\rm syn,0}\left(\frac{1+z}{1.022}\right)^{m_{12}} g(p)^{\frac{2(p-1)}{p+4}}\epsilon_{\rm e,-1}^{\frac{2(p-1)}{p+4}}\,A_k^{\frac{\alpha p+6\alpha-5p+30}{2(p+4)(\alpha+5-k)}} \times \epsilon_{B,-2}^{\frac{p+2}{2(p+4)}}\,\tilde{E}_{51}^{\frac{10p-kp-6k}{2(p+4)(\alpha+5-k)}}\,t_6^{m_{22}},$$
$$\nu_{\rm a,3}^{\rm syn} = \nu_{\rm a,3}^{\rm syn,0}\left(\frac{1+z}{1.022}\right)^{m_{13}}(1+Y)\,\epsilon_{B,-2}^{\frac{6}{5}}\,A_k^{\frac{3(3\alpha+10)}{5(\alpha+5-k)}} \times \tilde{E}_{51}^{\frac{15-9k}{5(\alpha+5-k)}}t_6^{m_{23}}, \quad (13)$$

where the PL indices m_{ij} for $i, j = 1, 2$, and 3 are explicitly shown in the Appendix.

Taking into account that the peak spectral power evolves as $P_{\nu,\rm max} \propto t^{-\frac{6+k\alpha}{2(\alpha+5-k)}}$ and the number of swept-up electrons in the post-shock develops as $N_{\rm e} \propto t^{\frac{6-2k+\alpha(3-k)}{\alpha+5-k}}$, the spectral peak flux density becomes

$$F_{\nu,\rm max}^{\rm syn} = F_{\nu,\rm max}^{\rm syn,0}\left(\frac{1+z}{1.022}\right)^{\frac{4+2k-4\alpha+3k\alpha}{2(\alpha+5-k)}}\epsilon_{B,-2}^{\frac{1}{2}}\,d_{z,26.5}^{-2}\,A_k^{\frac{3\alpha+7}{2(\alpha+5-k)}} \times \tilde{E}_{51}^{\frac{8-3k}{2(\alpha+5-k)}}\,t_7^{\frac{6-4k+6\alpha-3k\alpha}{2(\alpha+5-k)}}. \quad (14)$$

The terms $\gamma_{\rm m}^0$, $\gamma_{\rm c}^0$, $\nu_{\rm m}^{\rm syn,0}$, $\nu_{\rm c}^{\rm syn,0}$, and $F_{\nu,\rm max}^{\rm syn,0}$ are given in Table 1 for $k = 0$, 1, 1.5, 2, and 2.5.

Using the synchrotron break frequencies (Equation (12)) and the spectral peak flux density (Equation (14)), the synchrotron light curves in the fast- and slow-cooling regimes are

$$F_\nu^{\rm syn} \propto \begin{cases} t^{\frac{5+k+\alpha+k\alpha}{\alpha+5-k}}\,\nu^2, & \nu < \nu_{\rm a,3}^{\rm syn}, \\ t^{\frac{10-8k+11\alpha-6k\alpha}{3(\alpha+5-k)}}\,\nu^{\frac{1}{3}}, & \nu_{\rm a,3}^{\rm syn} < \nu < \nu_{\rm c}^{\rm syn}, \\ t^{\frac{10-4k+8\alpha-3k\alpha}{4(\alpha+5-k)}}\,\nu^{-\frac{1}{2}}, & \nu_{\rm c}^{\rm syn} < \nu < \nu_{\rm m}^{\rm syn}, \\ t^{-\frac{30p+kp(\alpha-8)-8(\alpha+5)+2k(\alpha+6)}{4(\alpha+5-k)}}\,\nu^{-\frac{p}{2}}, & \nu_{\rm m}^{\rm syn} < \nu, \end{cases} \quad (15)$$

$$F_\nu^{\rm syn} \propto \begin{cases} t^{\frac{2(\alpha+k-1)}{\alpha+5-k}}\,\nu^2, & \nu < \nu_{\rm a,1}^{\rm syn}, \\ t^{\frac{24+9\alpha-2k(2\alpha+5)}{3(\alpha+5-k)}}\,\nu^{\frac{1}{3}}, & \nu_{\rm a,1}^{\rm syn} < \nu < \nu_{\rm m}^{\rm syn}, \\ t^{-\frac{6(5p-2\alpha-7)+k(16+p(\alpha-8)+5\alpha)}{4(\alpha+5-k)}}\,\nu^{-\frac{p-1}{2}}, & \nu_{\rm m}^{\rm syn} < \nu < \nu_{\rm c}^{\rm syn}, \\ t^{-\frac{30p+kp(\alpha-8)-8(\alpha+5)+2k(\alpha+6)}{4(\alpha+5-k)}}\,\nu^{-\frac{p}{2}}, & \nu_{\rm c}^{\rm syn} < \nu, \end{cases} \quad (16)$$

and

$$F_\nu^{\rm syn} \propto \begin{cases} t^{\frac{2(\alpha+k-1)}{\alpha+5-k}}\,\nu^2, & \nu < \nu_{\rm m}^{\rm syn}, \\ t^{\frac{22+\alpha(k+8)}{4(\alpha+5-k)}}\,\nu^{\frac{5}{2}}, & \nu_{\rm m}^{\rm syn} < \nu < \nu_{\rm a,2}^{\rm syn}, \\ t^{-\frac{6(5p-2\alpha-7)+k(16+p(\alpha-8)+5\alpha)}{4(\alpha+5-k)}}\,\nu^{-\frac{p-1}{2}}, & \nu_{\rm a,2}^{\rm syn} < \nu < \nu_{\rm c}^{\rm syn}, \\ t^{-\frac{30p+kp(\alpha-8)-8(\alpha+5)+2k(\alpha+6)}{4(\alpha+5-k)}}\,\nu^{-\frac{p}{2}}, & \nu_{\rm c}^{\rm syn} < \nu, \end{cases} \quad (17)$$

respectively.

2.2.2. SSC Emission

The SSC break frequencies, the corresponding spectral peak flux density, and the light curves in the fast- and slow-cooling regimes are shown in the Appendix.

3. Analysis of the Multiwavelength Light Curves

3.1. Analysis of Synchrotron Light Curves

Figures 1–5 show the predicted synchrotron light curves produced by the deceleration of nonrelativistic ejecta in a circumstellar medium described by a density profile $A_k r^{-k}$ with $k = 0$, 1, 1.5, 2, and 2.5, respectively. The panels from top to bottom correspond to the electromagnetic bands in radio at 6 GHz, the optical at 1 eV, and X-rays at 1 keV for $\tilde{E} = 10^{51}$ erg, $\epsilon_B = 10^{-2}$, $\epsilon_{\rm e} = 10^{-1}$, and $d_z = 100$ Mpc. The left panels show the light curves for $p = 2.6$ with $\alpha = 3$, 4, and 5, and the right panels show the light curves for $\alpha = 3$ with $p = 2.2$, 2.8, and 3.4. All the figures lie in the slow-cooling regime and exhibit a deceleration timescale of several months to a few years due to the set of parameter values considered. Similar timescales have been observed in light curves from radio to hard X-rays in some SNe (e.g., SN 2014C and SN 2016aps; Margutti et al. 2017; Nicholl et al. 2020, respectively). If we chose another set of parameters such as a fiducial energy $\tilde{E} \simeq 10^{52}$ erg, a uniform-density medium $A_0 \simeq 10\,{\rm cm}^{-3}$, and equipartition parameters $\epsilon_{\rm e} \simeq 0.5$ and $\epsilon_B \simeq 0.1$, the synchrotron light curves would lie in the fast-cooling regime. Consequently, using a set of parameters such as $\tilde{E} \simeq 10^{47}$ erg, $A_2 \simeq 3 \times 10^{35}\,{\rm cm}^{-1}$, and $\beta = 0.5$ for $k = 2$ and $\tilde{E} \sim 10^{47}$ erg, $A_0 \simeq 1\,{\rm cm}^{-3}$, and $\beta = 0.5$ for $k = 0$, deceleration

Table 1
The Relevant Terms of the Free-coasting and Deceleration Phases

	$k=0$	$k=1.0$	$k=1.5$	$k=2.0$	$k=2.5$
A_k	$1\ \mathrm{cm}^{-3}$	$1.5\times10^{19}\ \mathrm{cm}^{-2}$	$2.7\times10^{28}\ \mathrm{cm}^{-\frac{3}{2}}$	$3\times10^{36}\ \mathrm{cm}^{-1}$	$1.3\times10^{45}\ \mathrm{cm}^{-\frac{1}{2}}$
Coasting Phase					
r^0 ($\times10^{17}$ cm)	2.2	1.8	1.5	1.3	1.1
$\gamma_{\rm m}^0$	12.4	12.4	12.4	12.4	12.4
$\gamma_{\rm c}^0$ ($\times10^3$)	3.1×10^2	1.8	0.3	0.8	0.5
$\nu_{\rm a,1}^{\rm syn,0}$(Hz)	2.9×10^9	1.3×10^{11}	5.5×10^{11}	2.9×10^{11}	6.4×10^{11}
$\nu_{\rm a,2}^{\rm syn,0}$(Hz)	1.0×10^8	2.5×10^9	8.1×10^9	4.7×10^9	7.7×10^9
$\nu_{\rm a,3}^{\rm syn,0}$(Hz)	1.5×10^6	6.5×10^9	9.3×10^{10}	2.6×10^{10}	7.5×10^{10}
$\nu_{\rm m}^{\rm syn,0}$(Hz)	3.5×10^6	4.6×10^7	1.1×10^8	6.8×10^7	8.3×10^7
$\nu_{\rm c}^{\rm syn,0}$(Hz)	2.9×10^{16}	7.3×10^{12}	2.8×10^{11}	1.7×10^{12}	8.2×10^{11}
$F_{\nu,\rm max}^{\rm syn,0}$ (mJy)	1.1×10^2	6.5×10^4	5.5×10^5	8.1×10^4	1.1×10^5
$\nu_{\rm mm}^{\rm ssc,0}$ (eV)	7.0×10^{-7}	9.2×10^{-6}	2.3×10^{-5}	1.4×10^{-5}	1.7×10^{-5}
$\nu_{\rm cc}^{\rm ssc,0}$(MeV)	3.8×10^6	3.2×10^{-2}	3.4×10^{-5}	1.5×10^{-3}	3.2×10^{-4}
$\nu_{\rm ma,1}^{\rm ssc,0}$(eV)	5.8×10^{-4}	2.6×10^{-2}	0.1	6.0×10^{-2}	0.1
$\nu_{\rm mc,1}^{\rm ssc,0}$(eV)	5.9×10^3	1.5	5.7×10^{-2}	0.3	0.2
$\nu_{\rm ma,2}^{\rm ssc,0}$(eV)	2.1×10^{-5}	5.1×10^{-4}	1.6×10^{-3}	9.5×10^{-4}	1.6×10^{-3}
$\nu_{\rm mc,2}^{\rm ssc,0}$(eV)	5.9×10^3	1.5	5.7×10^{-2}	0.3	0.2
$\nu_{\rm ca,2}^{\rm ssc,0}$(eV)	1.3×10^4	11.1	1.0	4.1	3.0
$\nu_{\rm ca,3}^{\rm ssc,0}$(eV)	1.9×10^2	28.4	11.4	22.9	29.3
$\nu_{\rm cm,3}^{\rm ssc,0}$(eV)	4.5×10^2	0.2	1.4×10^{-2}	5.9×10^{-2}	3.2×10^{-2}
$F_{\nu,\rm max}^{\rm ssc,0}$ (mJy)	5.8×10^{-5}	2.3	89.0	4.4	9.6
Deceleration					
t^0 ($\times10^3$ day)	1.2	1.1	1.4	28.4	7.0×10^3
r^0 ($\times10^{17}$ cm)	7.2	4.1	3.2	3.2	2.6
$\gamma_{\rm m}^0$ ($\times10^1$)	13.2	6.8	5.2	7.3	6.7
$\gamma_{\rm c}^0$($\times10^4$)	3.0	0.2	0.05	0.2	0.1
$\nu_{\rm a,1}^{\rm syn,0}$(Hz)	8.8×10^8	2.5×10^{10}	9.5×10^{10}	2.5×10^{10}	4.6×10^{10}
$\nu_{\rm a,2}^{\rm syn,0}$(Hz)	1.1×10^9	6.1×10^9	1.2×10^{10}	6.4×10^9	8.4×10^9
$\nu_{\rm a,3}^{\rm syn,0}$(Hz)	3.2×10^7	4.3×10^9	2.9×10^{10}	4.2×10^9	8.5×10^9
$\nu_{\rm m}^{\rm syn,0}$(Hz)	1.3×10^9	1.5×10^9	1.5×10^9	1.6×10^9	1.5×10^9
$\nu_{\rm c}^{\rm syn,0}$(Hz)	5.2×10^{14}	3.2×10^{12}	4.0×10^{11}	4.2×10^{12}	2.8×10^{12}
$F_{\nu,\rm max}^{\rm syn,0}$ (mJy)	1.3×10^4	3.8×10^5	1.3×10^6	1.3×10^5	1.0×10^5
$\nu_{\rm mm}^{\rm ssc,0}$(eV)	2.9×10^{-2}	8.8×10^{-3}	5.5×10^{-3}	1.1×10^{-2}	8.7×10^{-3}
$\nu_{\rm cc}^{\rm ssc,0}$(MeV)	6.0×10^2	1.0×10^{-2}	1.3×10^{-4}	1.8×10^{-2}	7.7×10^{-3}
$\nu_{\rm ma,1}^{\rm ssc,0}$(MeV)	2.0×10^{-2}	0.1	0.3	0.2	0.3
$\nu_{\rm mc,1}^{\rm ssc,0}$(MeV)	1.2×10^4	19.3	1.4	29.6	16.3
$\nu_{\rm ma,2}^{\rm ssc,0}$(MeV)	2.4×10^{-2}	3.7×10^{-2}	4.4×10^{-2}	4.5×10^{-2}	4.9×10^{-2}
$\nu_{\rm mc,2}^{\rm ssc,0}$(MeV)	1.2×10^4	19.3	1.4	29.6	16.3
$\nu_{\rm ca,2}^{\rm ssc,0}$(MeV)	1.2×10^3	19.6	4.0	28.2	23.2
$\nu_{\rm ca,3}^{\rm ssc,0}$(MeV)	36.7	14.0	9.2	18.5	23.4
$\nu_{\rm cm,3}^{\rm ssc,0}$(MeV)	1.6×10^3	10.2	0.9	7.0	2.2
$F_{\nu,\rm max}^{\rm ssc,0}$ (mJy)	2.1×10^{-2}	13.7	1.4×10^2	2.9	2.5

timescales of hours to months would be obtained. This is also the case where the ejecta mass is decelerated in a very dense medium (for a discussion, see Chevalier & Irwin 2011; Nicholl et al. 2020).

A density profile $n(r)=A_k r^{-k}$ with $k=0$, 1, 1.5, 2, and 2.5 for a circumstellar medium that covers sGRB and lGRB progenitors is used. While the uniform-density medium ($k=0$) is expected to be connected with binary compact objects and CC-SNe, the stratified medium ($1\leqslant k\leqslant 2.5$) is only expected to be associated with dying massive stars with different mass-loss evolutions. For instance, Yi et al. (2013) and Liang et al. (2013) studied the dynamics of synchrotron external-shock emission in a sample of 19 and 146 GRBs and found that they were successfully described when the outflow was decelerated in an external environment with $0.4\leqslant k\leqslant 1.4$ and $k\approx 1$, respectively. Izzo et al. (2020) presented multiwavelength observations of the nearby SN 2020bvc. The authors found that the X-ray observations were consistent with the afterglow emission generated by an off-axis jet with a viewing angle of 23° when it was decelerated in a circumburst medium with a density profile with $k=1.5$.

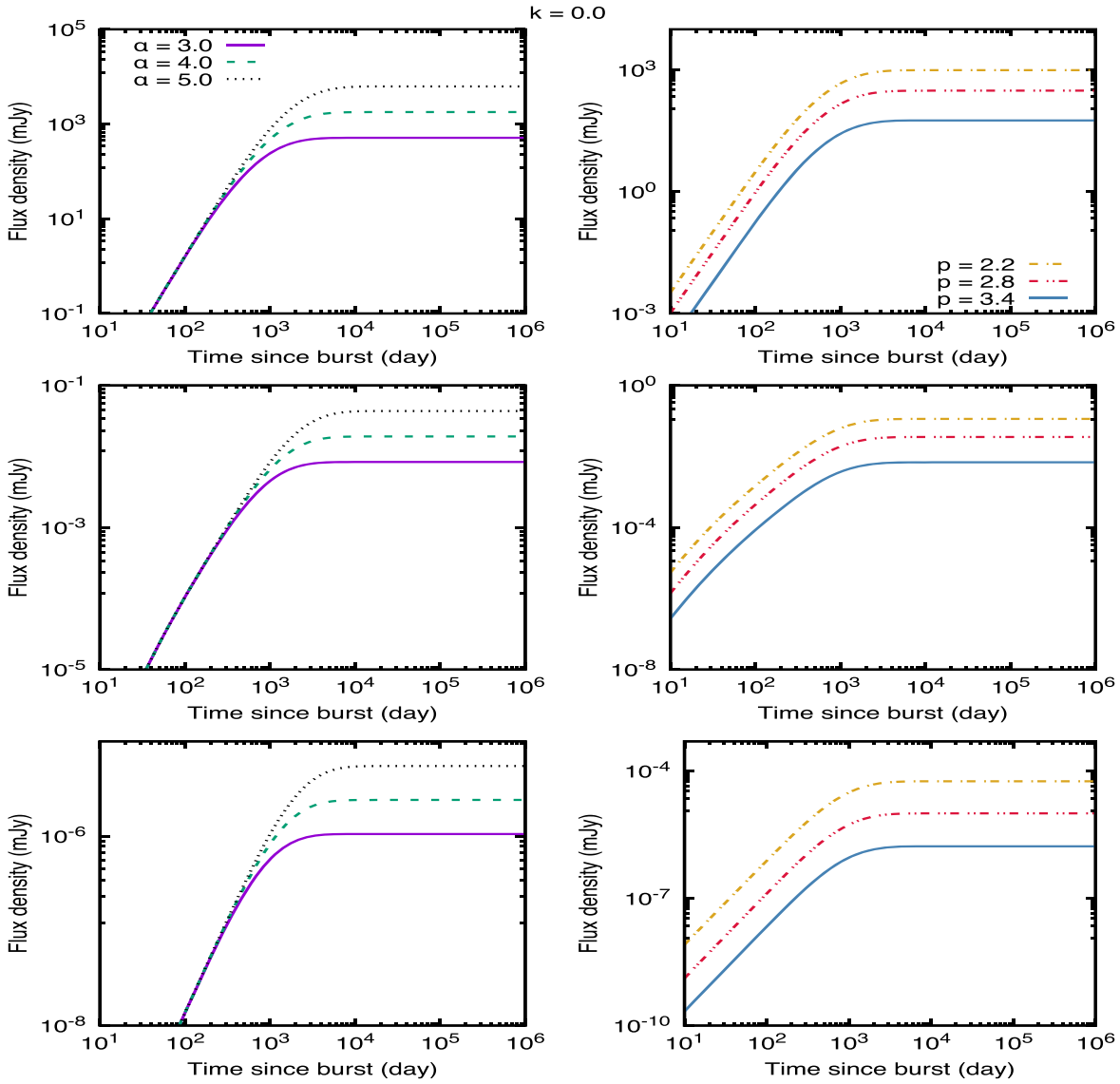

Figure 1. Synchrotron light curves generated by the deceleration of the nonrelativistic ejecta for $k = 0$. The panels from top to bottom correspond to radio (1.6 GHz), optical (1 eV), and X-ray (1 keV) bands. The left panels show the light curves for $p = 2.6$ with $\alpha = 3$, 4, and 5, and the right panels show the light curves for $\alpha = 3$ with $p = 2.2$, 2.8, and 3.4. The following parameters are used: $\tilde{E} = 10^{51}$ erg, $A_0 = 1$ cm^{-3}, $\epsilon_B = 10^{-2}$, $\epsilon_e = 10^{-1}$, and $d = 100$ Mpc.

Figure 1 shows that during the coasting phase, the flux increases gradually, and during the deceleration phase, depending on the values of α and p, a flattening or decrease in the light curve is expected. Figures 2–5 show that for a density profile with $1 < k \leqslant 2.5$ the rebrightening in the light curves is not so evident. Therefore, a flattening or rebrightening at timescales of months to years in the light curves together with gravitational wave (GW) detection would be associated with the deceleration of nonrelativistic ejecta launched during the coalescence of binary compact objects or a CC-SN. Even a flattening or rebrightening at timescales of days could be detected with extreme values of circumstellar density or fiducial energy. Additionally, it can be concluded that an observed flux that decreases early would be associated with the deceleration of nonrelativistic ejecta launched by dying massive stars with different mass-loss evolutions (the mass-loss rate $\dot{M}$ and/or the wind velocity v_w) at the end of their life (Ramirez-Ruiz et al. 2005; van Marle et al. 2006).

The synchrotron light curve in the slow-cooling regime as a function of the density parameter during the deceleration phase is given by

$$F_\nu^{\rm syn} \propto \begin{cases} A_k^{-\frac{4}{\alpha+5-k}}, & \nu < \nu_{\rm a,1}^{\rm syn}, \\ A_k^{\frac{4\alpha+13}{3(\alpha+5-k)}}, & \nu_{\rm a,1}^{\rm syn} < \nu_{\rm m}^{\rm syn}, \\ A_k^{\frac{19+p(\alpha-5)+5\alpha}{4(\alpha+5-k)}}, & \nu_{\rm m}^{\rm syn} < \nu < \nu_{\rm c}^{\rm syn}, \\ A_k^{\frac{p(\alpha-5)+2(\alpha+5)}{4(\alpha+5-k)}}, & \nu_{\rm c}^{\rm syn} < \nu. \end{cases} \quad (18)$$

The predicted flux is less sensitive to the density parameter for higher frequencies than for lower ones (e.g., the radio light curve is more sensitive to variations of the density parameter than the X-ray light curve). It can also be noted that the predicted flux is more sensitive to the density parameter for larger values of k and α. It is worth noting that a transition phase from a stellar-wind ($k = 2$) to a uniform-density ($k = 0$) medium would be more evident in lower-frequency fluxes (e.g., this transition is more noticeable in radio or optical bands than in X-ray bands). A similar signature is useful for describing the type of progenitor, the mass-loss evolution, and the afterglow

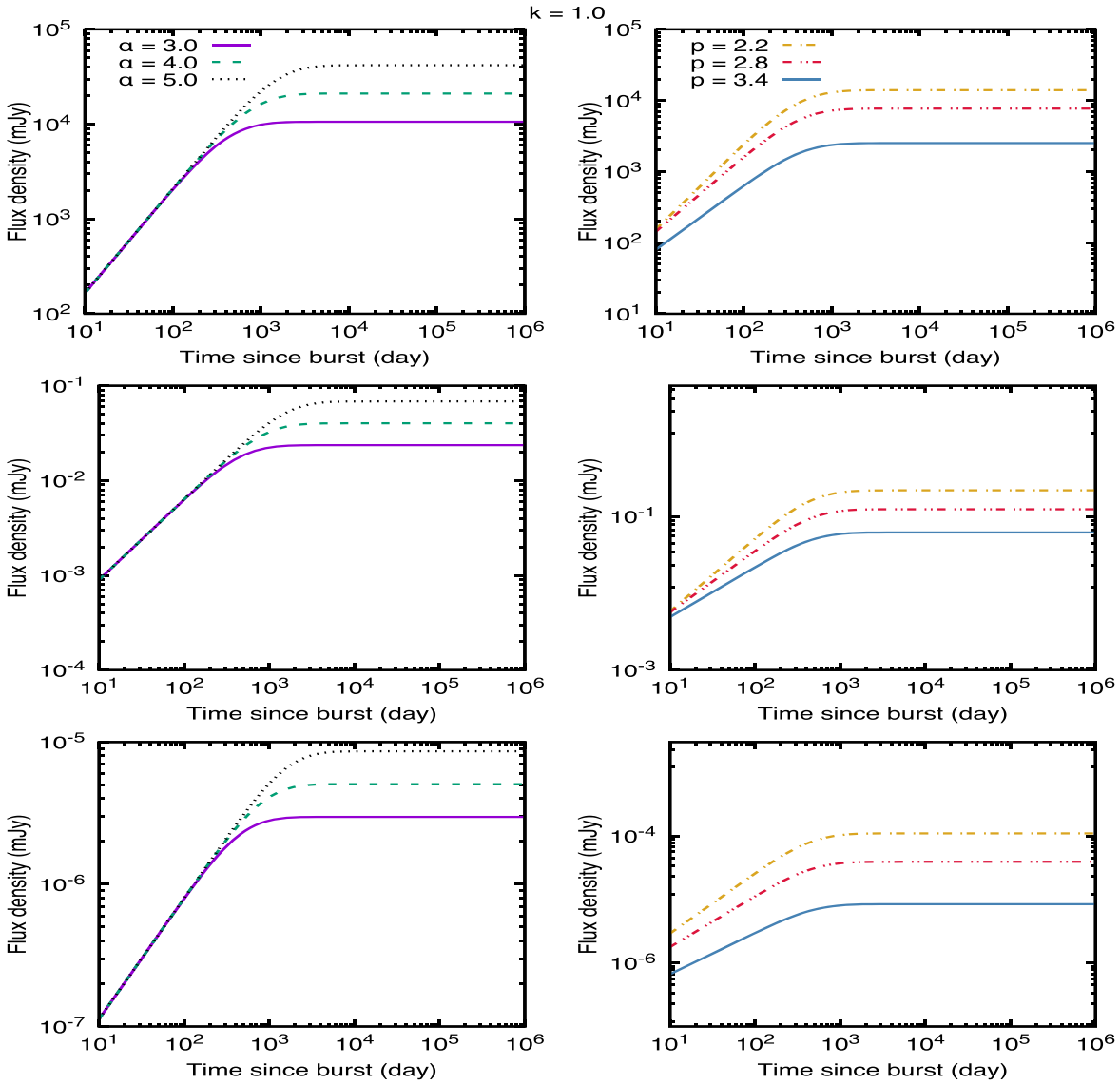

Figure 2. Same as Figure 1, but for $k = 1.0$ with $A_1 = 1.5 \times 10^{19}$ cm^{-2}.

emission by the deceleration of the relativistic jet and also for estimating the transition radius at ∼(0.1–1) pc of some bursts (e.g., see GRB 050319, 080109A, 160625B, and 190114C; Kamble et al. 2007; Jin et al. 2009; Fraija et al. 2017, 2019b).

Figures 1–5 show the synchrotron light curves for distinct values of p and α and the same values of the microphysical parameters $\epsilon_B = 10^{-2}$ and $\epsilon_e = 10^{-1}$. However, any variation of the microphysical parameters will increase or decrease the predicted fluxes. For example, the synchrotron light curve in the slow-cooling regime as a function of these parameters evolves as $F_\nu^{\rm syn}$: $\propto \epsilon_e^{-\frac{2}{3}}\,\epsilon_B^{\frac{1}{3}}$ for $\nu < \nu_m^{\rm syn}$, $\propto \epsilon_e^{p-1}\,\epsilon_B^{\frac{p+1}{4}}$ for $\nu_m^{\rm syn} < \nu < \nu_c^{\rm syn}$, and $\propto \epsilon_e^{p-1}\,\epsilon_B^{\frac{p-2}{4}}$ for $\nu_c^{\rm syn} < \nu$. The expected flux is more sensitive to the parameter ϵ_B for lower frequencies than for higher ones and to the parameter ϵ_e for higher frequencies than for lower ones.

The synchrotron spectral breaks during the nonrelativistic regime evolve as $\nu_m^{\rm syn} \propto t^{-\frac{k}{2}}$ and $\nu_c^{\rm syn} \propto t^{\frac{3k-4}{2}}$ in the coasting phase and as $\nu_m^{\rm syn} \propto t^{-\frac{30+k(\alpha-8)}{2(\alpha+5-k)}}$ and $\nu_c^{\rm syn} \propto t^{\frac{k(4+3\alpha)-4\alpha-2}{2(\alpha+5-k)}}$ in the deceleration phase. For instance, these breaks evolve as $\nu_m^{\rm syn} \propto t^0$ and $\nu_c^{\rm syn} \propto t^{-2}$ in the coasting phase and as $\nu_m^{\rm syn} \propto t^{-3}$ and $\nu_c^{\rm syn} \propto t^{-\frac{1}{3}}$ in the deceleration phase for a uniform-density medium and as $\nu_m^{\rm syn} \propto t^{-1}$ and $\nu_c^{\rm syn} \propto t$ in the coasting phase and as $\nu_m^{\rm syn} \propto t^{-\frac{7}{3}}$ and $\nu_c^{\rm syn} \propto t$ in the deceleration phase for a stellar-wind medium. Here, we present a valuable tool for pinpointing emission from nonrelativistic ejecta as previously done by Giblin et al. (1999) in the case of the relativistic regime. Giblin et al. (1999) analyzed the prompt gamma-ray emission in the BATSE-detected[14] burst GRB 980923. The light curve exhibited a main prompt episode lasting ∼40 s followed by a smooth emission tail that lasted ∼400 s. The authors found that the spectrum in the smooth tail evolved with the synchrotron cooling break $\propto t^{-0.52\pm0.12}$, concluding that the afterglow began during the prompt gamma-ray emission. Later, spectral analysis of GRB tails was done in order to identify early afterglows (e.g., see Barthelmy et al. 2005; Yamazaki et al. 2006).

[14] Burst and Transient Source Experiment.

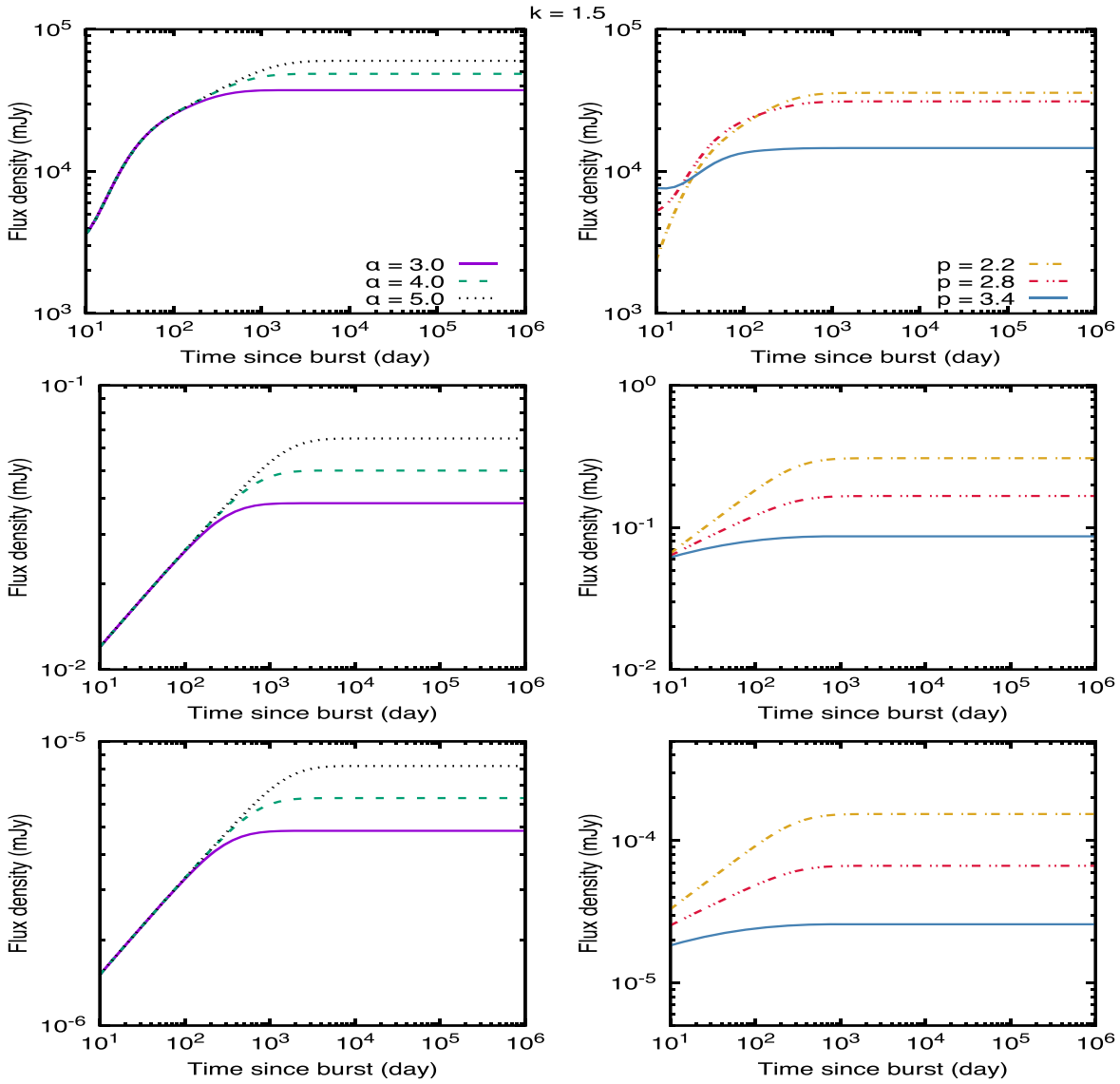

Figure 3. Same as Figure 1, but for $k = 1.5$ with $A_{1.5} = 2.7 \times 10^{28}\,\mathrm{cm}^{-\frac{3}{2}}$.

3.2. Analysis of SSC Light Curves

Figure 6 shows the predicted SSC light curves at 100 keV (upper), 10 GeV (middle), and 100 GeV (lower) for the deceleration of the nonrelativistic ejecta mass in a circumstellar medium with a density profile $A_k r^{-k}$ with $k = 0$, 1, 1.5, 2, and 2.5. The left panels show the light curves for $p = 2.4$ and $\alpha = 3$, and the right panels those for $p = 2.8$ and $\alpha = 5$. In order to obtain the SSC light curves, we use the same typical values that are used for the synchrotron light curves. The effect of the extragalactic background light (EBL) absorption modeled in Franceschini & Rodighiero (2017) is used.

The purple solid line ($k = 0$) in Figure 6 shows that a flattening or rebrightening in the light curve is expected, but not in a density profile with $k > 1$. This feature at timescales of months to years together with GW detection would be associated with the deceleration of nonrelativistic ejecta launched during the coalescence of a binary compact object or a CC-SN. In contrast, it is expected that an observed flux that decreases early would be associated with the deceleration of nonrelativistic ejecta launched in the collapse of massive stars with different mass-loss evolutions at the end of their life (Ramirez-Ruiz et al. 2005; van Marle et al. 2006).

The SSC light curve in the slow-cooling regime as a function of the density parameter during the deceleration phase can be written as

$$F_\nu^{\rm ssc} \propto \begin{cases} A_k^{\frac{9(\alpha+5)}{5(\alpha+5-k)}}, & \nu < \nu_{\rm a,1}^{\rm ssc}, \\ A_k^{\frac{29+7\alpha}{3(\alpha+5-k)}}, & \nu_{\rm a,1}^{\rm ssc} < \nu_{\rm m}^{\rm ssc}, \\ A_k^{\frac{43+p(\alpha-13)+9\alpha}{4(\alpha+5-k)}}(C_1 + C_2 \ln A_k^{-\frac{7(\alpha+3)}{2(\alpha+5-k)}}), & \nu_{\rm m}^{\rm ssc} < \nu < \nu_{\rm c}^{\rm ssc}, \\ A_k^{\frac{22-13p+2\alpha+\alpha p}{4(\alpha+5-k)}}(C_3 + C_4 \ln A_k^{\frac{7(\alpha+3)}{2(\alpha+5-k)}}), & \nu_{\rm c}^{\rm ssc} < \nu. \end{cases} \quad (19)$$

The parameters C_s do not evolve with the density parameter. Considering that the contribution from the logarithm function is small, this light curve has a similar behavior to the synchrotron light curves.

Inverse Compton (IC) scattering between an electron distribution accelerated during the shock wave and the photon

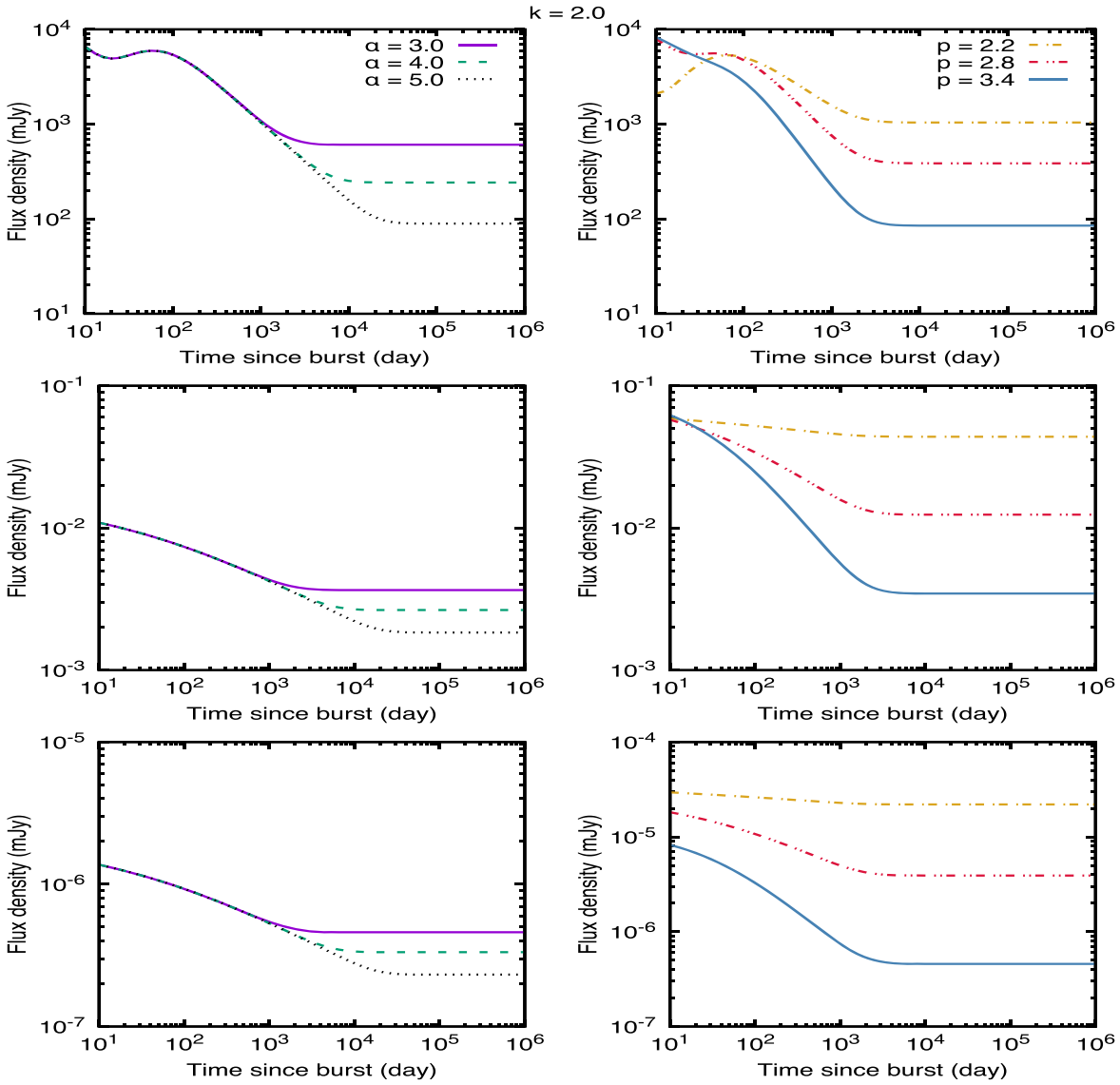

Figure 4. Same as Figure 1, but for $k = 2.0$ with $A_2 = 3 \times 10^{36}$ cm^{-1}.

field from SNe has been explored in order to explain the X-ray emission observed in timescales of days after the explosion (Björnsson & Fransson 2004; Chevalier et al. 2006; Chevalier & Fransson 2006; Margutti et al. 2013). Björnsson & Fransson (2004) studied the X-ray and radio emission from SN 2002ap. The authors proposed that IC scattering could explain the X-ray excess observed at late times. They computed that the IC spectrum 6 days after the explosion peaks at energies of some megaelectronvolts. Chevalier & Fransson (2006) found that although IC emission could reproduce the X-ray flux observed in SN 2002ap for a spectral index of $p = 3$, this process is not promising for other SNe unless the electron energy density is much higher than the magnetic energy density. On the other hand, Margutti et al. (2012) introduced an analytic formalism for IC scattering in the X-ray energy range and in an SN scenario with compact progenitors. They showed that IC luminosity evolves as $\propto t^{1.29-0.58p}$ for a uniform-density medium and as $\propto t^{-(0.24p+0.64)}$ for a wind medium. In this paper, we propose that in addition to the external IC scattering process, an SSC mechanism could be present. Figure 6 shows that in a density profile with $k > 1$, an SSC flux could be detected in timescales of days with the evolution given by Equations (A14) and (A15). For instance, the SSC fluxes in the slow-cooling regime evolve as $\propto t^{\frac{4\alpha+14}{\alpha+5}}$ for $\nu < \nu_{\rm m}^{\rm ssc}$, as $\propto t^{\frac{37-27p+8\alpha}{2(\alpha+5)}}$ for $\nu_{\rm m}^{\rm ssc} < \nu < \nu_{\rm c}^{\rm ssc}$, and as $\propto t^{\frac{38-27p+4\alpha}{2(\alpha+5)}}$ for $\nu_{\rm c}^{\rm ssc} < \nu$ for a uniform-density medium and as $\propto t^{\frac{2(1-\alpha)}{3(\alpha+3)}}$ for $\nu < \nu_{\rm m}^{\rm ssc}$, as $\propto t^{\frac{5-\alpha-p(\alpha+11)}{2(\alpha+3)}}$ for $\nu_{\rm m}^{\rm ssc} < \nu < \nu_{\rm c}^{\rm ssc}$, and as $\propto t^{\frac{14-11p+\alpha(2-p)}{2(\alpha+3)}}$ for $\nu_{\rm c}^{\rm ssc} < \nu$ for a stellar-wind medium, which have a different evolution from the IC scattering model derived in Margutti et al. (2012).

4. Nonrelativistic Masses Ejected from the Coalescence of an NS Binary

NS mergers are widely accepted to launch significant masses with different velocities that will contribute at distinct timescales, frequencies, and intensities. Once these ejecta masses move into the circumstellar medium, the initial expansion phase is not affected until the swept-up quantity of material is equal to the ejected masses. In this moment, the ejecta masses start to decelerate. The nonrelativistic masses ejected from NS mergers are dynamical ejecta, cocoon

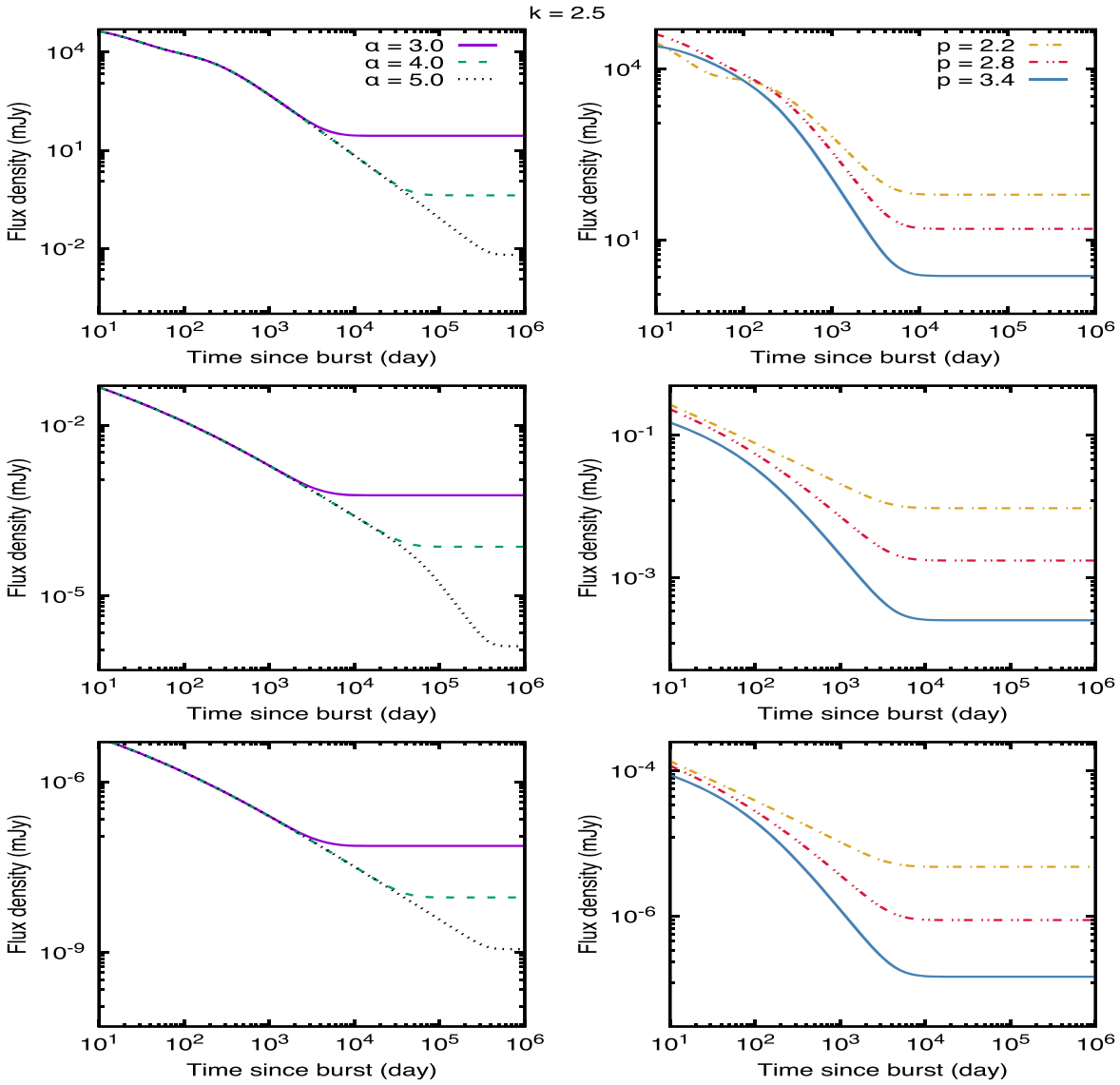

Figure 5. Same as Figure 1, but for $k = 2.5$ with $A_{2.5} = 1.3 \times 10^{45}\,\mathrm{cm}^{-\frac{1}{2}}$.

material, shock breakout material, and wind ejecta. As follows we give a brief introduction of each of these ejecta masses.

4.1. Dynamical Ejecta

Dynamical ejecta is formed during coalescence due to hydrodynamical and gravitational interactions (Davies et al. 1994; Ruffert et al. 1997; Rosswog et al. 1999). Based on numerical simulations, the ejecta mass liberated, the kinetic energy, and the velocities lie in the ranges of $10^{-4} \lesssim M_{\rm ej} \lesssim 10^{-2}\,M_{\odot}$, $10^{49} \lesssim E \lesssim 10^{51}$ erg, and $0.1 \lesssim \beta\Gamma \lesssim 0.3$, respectively (e.g., see Goriely et al. 2011; Bauswein et al. 2013; Hotokezaka et al. 2013; Piran et al. 2013; Grossman et al. 2014; Wanajo et al. 2014).

4.2. Cocoon Material

As the GRB jet makes its way through the neutrino-driven or magnetically driven wind (previously ejected during the NS merger), it deposits energy around its way. The energy deposited laterally forms a cocoon, which may have an energy comparable to that of the electromagnetic emission created by the jet. Murguia-Berthier et al. (2014) studied the necessary conditions for cocoon production as a function of the jet luminosity. The authors found that when the jet has a low (high) luminosity, a weak cocoon emission is expected. Nagakura et al. (2014) numerically showed that when a low-luminosity jet is considered, a hot cocoon confining the jet is formed. As soon as the relativistic jet reaches the shock breakout material, the cocoon breaks out and expands along the jet's axis. Beyond the breakout material, external pressure decreases abruptly, so the cocoon can accelerate and expand relativistically until it becomes transparent. Accelerated material from the cocoon fireball will continue moving in the jet's axis. It is worth mentioning that the significance of the cocoon also depends on the delay time between the merger and jet launching (Geng et al. 2019). The ejecta mass liberated in the cocoon, the kinetic energy, and the velocities lie in the ranges of $10^{-6} \lesssim M_{\rm ej} \lesssim 10^{-4}\,M_{\odot}$, $10^{47} \lesssim E \lesssim 10^{50.5}$ erg, and $0.2 \lesssim \beta\Gamma \lesssim 10$, respectively (e.g., see Murguia-Berthier et al. 2014; Nagakura et al. 2014; Lazzati et al. 2017, 2018; Nakar & Piran 2017; Gottlieb et al. 2018).

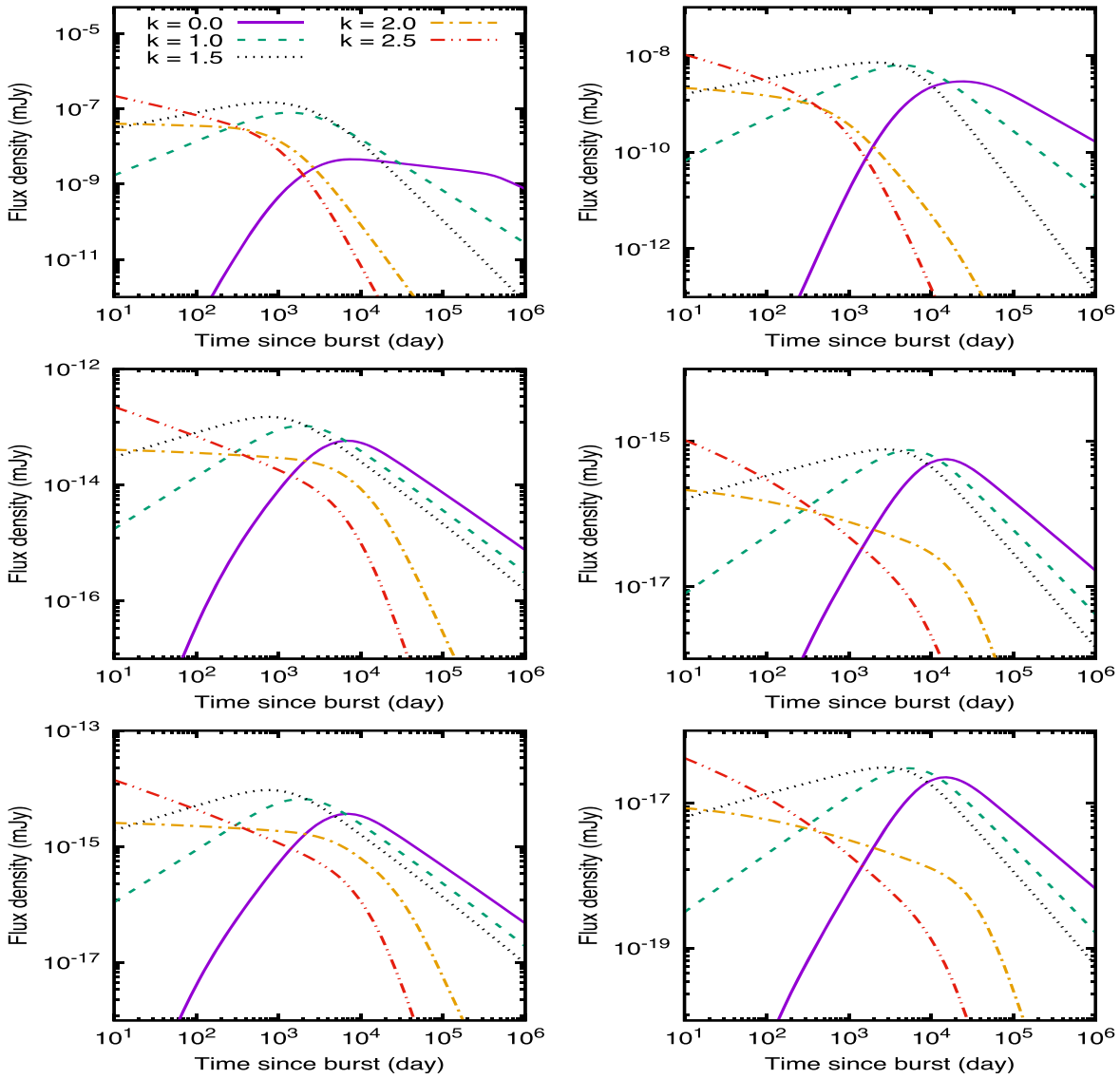

Figure 6. SSC light curves generated by the deceleration of the nonrelativistic ejecta for $k = 0$, 1, 1.5, 2, and 2.5. The panels from top to bottom correspond to gamma-ray fluxes at 100 keV, 10 GeV, and 100 GeV, respectively. The left panels show the light curves for $p = 2.4$ and $\alpha = 3.0$, and the right panels those for $p = 2.8$ and $\alpha = 5.0$. We use the same typical values that are used for the synchrotron light curves.

4.3. Shock Breakout Material

The shock breakout material's properties depend on the mass, radius, and velocity of the merger remnant. Immediately after coalescence occurs, a shock formed at the interface between the two NSs is initially ejected from the NS core to the NS crust at subrelativistic velocities ($\beta_{\rm in} \simeq 0.25$; e.g., see Kyutoku et al. 2014; Metzger et al. 2015). Once the shock reaches half of the escape velocity, a fraction of the thermal energy is converted into kinetic energy and it can leave the merger (for details see Kyutoku et al. 2014; Fraija et al. 2019d). Numerical simulations indicate that the ejecta mass, the kinetic energy, and the velocities lie in the ranges of $10^{-6} \lesssim M_{\rm ej} \lesssim 10^{-4}\, M_\odot$, $10^{47} \lesssim E \lesssim 10^{50.5}$ erg, and $\beta\Gamma \gtrsim 0.8$, respectively (e.g., see Kyutoku et al. 2014; Metzger et al. 2015).

4.4. Disk Wind Ejecta

The coalescence of an NS binary will finish in a tidal disruption, resulting in the formation of an accretion disk around the central remnant. The accretion disk will have a mass in the range of $10^{-3} \lesssim M_{\rm ej} \lesssim 0.3\, M_\odot$ (Shibata & Taniguchi 2006; Hotokezaka et al. 2013), and due to a large source of thermal neutrinos (Popham et al. 1999), it could generate an outflow driven by neutrino heating similar to neutrino-driven proto-NS winds in CC-SNe (Metzger et al. 2008; Surman et al. 2008). It represents a significant source of ejecta mass that might even dominate other ejecta masses as suggested by Siegel & Metzger (2017). The ejecta mass, the kinetic energy, and the velocities lie in the ranges of $10^{-4} \lesssim M_{\rm ej} \lesssim 10^{-1.3}\, M_\odot$, $10^{47} \lesssim E \lesssim 10^{50}$ erg, and $0.03 \lesssim \beta\Gamma \lesssim 0.1$, respectively (e.g., see Dessart et al. 2009; Metzger & Fernández 2014; Fernández et al. 2015).

4.5. Analysis of the Multiwavelength Light Curves

Figure 7 shows the synchrotron and SSC light curves generated by nonrelativistic masses ejected from the coalescence

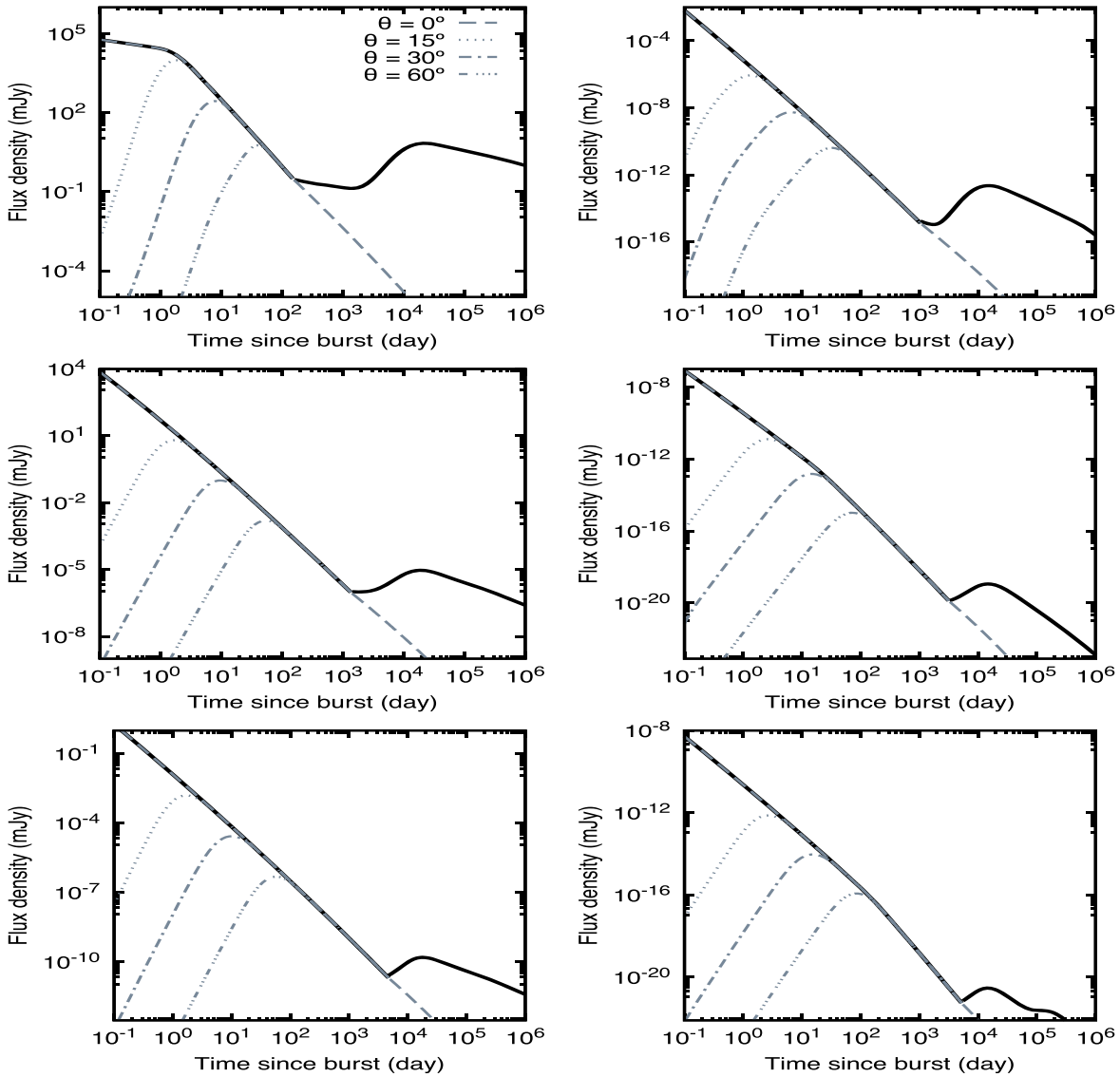

Figure 7. SSC and synchrotron light curves generated by nonrelativistic masses ejected from NS mergers, such as dynamical ejecta, the cocoon, shock breakout, and wind. The left panels show the synchrotron light curves that correspond to (from top to bottom) the radio (1.6 GHz), optical (1 eV), and X-ray (1 keV) bands, and the right panels show the SSC light curves that correspond to (from top to bottom) the gamma-ray fluxes at 100 keV, 10 GeV, and 100 GeV. The following parameters are used: $A_0 = 1$ cm^{-3}, $p = 2.6$, $\alpha = 3.0$, $\epsilon_B = 10^{-1}$, $\epsilon_e = 10^{-1}$, and $d = 100$ Mpc. The gray solid lines correspond to on-axis and off-axis relativistic jets with viewing angles of $\theta = 15°$, 30°, and 60°. The black solid line represents the total contribution from the relativistic jet and the nonrelativistic masses ejected from NS mergers. The expected fluxes from the relativistic jet are obtained in accordance with the afterglow model introduced in Fraija et al. (2019c).

of an NS binary, including dynamical ejecta, cocoon material, shock breakout material, and wind ejecta.[15] Electromagnetic emission from the nonrelativistic masses is shown as a bump at a timescale of $\geqslant 10^3$ days. In addition, we consider the synchrotron and SSC emission from on-axis and off-axis relativistic jets with viewing angles of $\theta = 15°$, 30°, and 60°.[16] The light curves corresponding to the off-axis jet are plotted in accordance with the afterglow model introduced in Fraija et al. (2019c). The left panels show the synchrotron light curves that correspond to (from top to bottom) the radio (1.6 GHz), optical (1 eV), and X-ray (1 keV) bands, and the right panels show the SSC light curves that correspond to (from top to bottom) the gamma-ray fluxes at 100 keV, 10 GeV, and 100 GeV. The coalescence of the two NSs launches significant nonrelativistic masses with different velocities that will contribute at distinct timescales, frequencies, and intensities. These ejecta masses interact with the circumstellar medium, generating nonthermal emission. The predicted synchrotron fluxes generated from (i) the shock breakout material peak at timescales of hours to days, (ii) those from the cocoon material peak at timescales of weeks to months, (iii) those from the dynamical ejecta peak at years, and (iv) those from the disk wind ejecta peak at centuries. Similar timescales with different intensities are shown in the SSC light curves.

This figure shows that the afterglow emission originating from the deceleration of the on-axis relativistic jet would have to decrease so that electromagnetic emission from the nonrelativistic masses could be observed. Murguia-Berthier et al. (2014) and Nagakura et al. (2014) estimated the necessary conditions for sGRB production in the coalescence of an NS

[15] The pair of values ($\tilde{E} = 10^{50}$ erg; $\beta = 0.2$) is used for the dynamical ejecta, (10^{48} erg; 0.3) for the cocoon material, ($10^{48.5}$ erg; 0.8) for the shock breakout material, and (10^{50} erg; 0.07) for the wind. All light curves shown are for $n = 1$ cm^{-3}, $\alpha = 3$, $\epsilon_B = 10^{-2}$, $\epsilon_e = 10^{-1}$, $p = 3.2$, and $d_z = 100$ Mpc.

[16] Values of $\tilde{E} = 10^{50}$ erg, $\epsilon_B = 10^{-2}$, $\epsilon_e = 10^{-1}$, $n = 10^{-2}$ cm^{-3}, $p = 2.2$, and $d_z = 100$ Mpc are used for the relativistic jet.

binary. In the case where such conditions are not satisfied, a relativistic jet is not expected, and electromagnetic emission from nonrelativistic masses could be observed from early times.

Because shock breakout material is described to have a velocity of $\beta = 0.8$ (Metzger et al. 2015), the transrelativistic regime introduced in Huang et al. (1998) is used. In this regime, the kinetic energy of the shock in the uniform-density medium is given by $E_{\rm K} = \frac{4\pi}{3}\sigma m_{\rm p} c^2 \beta^2 \Gamma^2 r^3 n$ (Blandford & McKee 1976) with $\sigma = 0.73$–0.38β and $r \approx \beta t$ (Huang et al. 1998). Taking this regime into account, the equivalent kinetic energy distribution is $E = \tilde{E}(\beta\Gamma)^{-\alpha}$, and the deceleration time becomes

$$t_{\rm dec} = \left(\frac{3}{4\pi\sigma m_{\rm p} c^5}\right)^{\frac{1}{3}} (1+z) A_0^{-\frac{1}{3}} \tilde{E}^{\frac{1}{3}} \beta^{-\frac{\alpha+5}{3}} \Gamma^{-\frac{\alpha+2}{3}}. \quad (20)$$

In the transrelativistic regime, the velocity obtained from Equation (20) is used to find the synchrotron and SSC quantities. It is worth noting that in the limit $\Gamma \to 1$, Equations (8) and (10) are recovered.

In the "deep Newtonian" regime the Lorentz factor of the lowest-energy electrons is $\gamma_{\rm m} \simeq 2$ (Sironi & Giannios 2013; Kathirgamaraju et al. 2016; Margalit & Piran 2020). Using Equation (11), the deceleration time in this regime becomes

$$t_{\rm DN} \simeq 2 \times 10^5 \,{\rm days} \left(\frac{1+z}{1.022}\right) \epsilon_{\rm e,-1}^{\frac{\alpha+5}{6}} A_0^{-\frac{1}{3}} \tilde{E}_{51}^{\frac{1}{3}}, \quad (21)$$

and the velocity of the ejecta is $\beta \simeq 0.05$. In this case the characteristic break frequency evolves as $\nu_{\rm m}^{\rm syn} \propto t^{-\frac{3}{\alpha+5}}$, the spectral peak flux density as $F_{\nu,\rm max}^{\rm syn} \propto t^{\frac{3(\alpha-1)}{\alpha+5}}$, and the predicted flux as $F_\nu = F_{\nu,\rm max}^{\rm syn} \left(\frac{\nu}{\nu_{\rm m}}\right)^{-\frac{p-1}{2}} \propto t^{-\frac{3(1+p-\alpha)}{2(\alpha+5)}} \nu^{-\frac{p-1}{2}}$ for $\nu_{\rm m}^{\rm syn} < \nu < \nu_{\rm c}^{\rm syn}$. Therefore, it is worth noting that due to the range of velocities considered ($0.07 \leqslant \beta \leqslant 0.8$) and the deceleration timescales, the deep Newtonian regime is only required for the wind ejecta. The coalescence of the NS binaries launches significant nonrelativistic masses with different velocities that will contribute at distinct timescales, frequencies, and intensities. These nonrelativistic masses interact with the circumstellar medium, generating nonthermal electromagnetic emission. We calculate the expected gamma-ray, X-ray, optical, and radio fluxes via SSC and synchrotron emission from electrons accelerated in the forward shocks. These electromagnetic signatures at different timescales and frequencies would be similar to those detected around SNe for a uniform-density medium and would also be present together with GW detections.

5. Nonrelativistic Masses Ejected from the Core Collapse of Dying Massive Stars

The origin of lGRBs is widely accepted to be connected to the death of massive stars leading to SNe, where afterglow emission from bursts is detected together with an SN Ic with broad lines (e.g., see Woosley & Janka 2005; Cano et al. 2017). Sub-energetic GRBs are believed to be quasi-spherical explosions dominated by nonrelativistic ejecta masses. The nonrelativistic material carries ≈99.9% of the explosion energy, and the mildly relativistic ejecta only ≈0.1%. The energy carried by the nonrelativistic ejecta is similar to that exhibited by sub-energetic bursts and comparable to that of the most energetic SNe Ib/c. Margutti et al. (2014) showed the equivalent kinetic energy profile as a function of ejecta mass velocity in the nonrelativistic and relativistic regimes of ordinary SNe Ibc, engine-driven SNe, sub-energetic GRBs, and relativistic SNe. The velocity of the ejecta mass was divided into a nonrelativistic phase $0.02 \lesssim \beta \lesssim 0.3$, a mildly relativistic phase $\Gamma\beta \approx 0.6$–0.8, and a relativistic phase $2 \lesssim \beta \lesssim 20$. It is worth noting that the broadened lines in their spectra indicate that a diverse range of materials with distinct nonrelativistic expansion velocities were present (e.g., O_{II}, N_{II}, S_{II}, etc.; Modjaz et al. 2020).

Depending on the range of values in the observables, such as the luminosity, duration, and bulk Lorentz factor, lGRBs could be successful or choked (e.g., see MacFadyen et al. 2001; Mészáros & Waxman 2001; Bromberg et al. 2011; Fraija 2014; Sobacchi et al. 2017). Choked GRBs might be more frequent than successful ones, only limited by the ratio of SN rates (Types Ib/c and II) to lGRB rates (Totani 2003; Ando & Beacom 2005). Some SNe of Type Ic-BL not connected with GRBs have been suggested to arise from events such as off-axis GRBs or failed jets (e.g., see Izzo et al. 2019, 2020; Beniamini et al. 2020). This is the case of the failed burst GRB 171205A, which besides being associated with SN 2017iuk exhibited material with high expansion velocities $\beta \sim 0.4$, interpreted as mildly relativistic cocoon material (Izzo et al. 2019). Izzo et al. (2020) found that X-ray observations from the nearby SN 2020bvc were consistent with the afterglow emission generated by an off-axis jet with a viewing angle of 23° when it decelerated in a circumburst medium with a density profile with $k = 1.5$.

Figure 8 shows the synchrotron and SSC light curves when the nonrelativistic ejecta mass decelerates in a stratified wind medium. The light curves corresponding to the off-axis jet are plotted in accordance with the afterglow model introduced in Fraija et al. (2019c). The left panels show the synchrotron light curves that correspond to (from top to bottom) the radio (1.6 GHz), optical (1 eV), and X-ray (1 keV) bands, and the right panels show the SSC light curves that correspond to (from top to bottom) the gamma-ray fluxes at 100 keV, 10 GeV, and 100 GeV. This figure shows that the afterglow emission originating from the deceleration of the on-axis relativistic jet would have to decrease so that afterglow emission from the nonrelativistic ejecta could be observed.

In our model, the afterglow emission from the nonrelativistic ejecta in the radio band is observed as a flaring event, while the afterglow from the optical and X-ray bands is seen as tails. The figure shows that, depending on the parameters and the viewing angle, the afterglow emission from the nonrelativistic ejecta can be detected at early times. Similarly, when the jet is choked, the afterglow emission from the nonrelativistic ejecta can be observed at early times.

Electromagnetic emission from the nonrelativistic ejecta and the relativistic jet could be distinguished, for example, through the evolution of the synchrotron flux derived in Equations (5) and (7) for the coasting phase and that derived in Equations (15) and (19) for the deceleration phase.

In order to analyze mildly relativistic SNe with velocities in the range of $\Gamma\beta \approx 0.6$–0.8, such as SN 2012ap, the synchrotron process in the transrelativistic regime as discussed in Section 4.5 for shock breakout material through Equation (20) would be required.

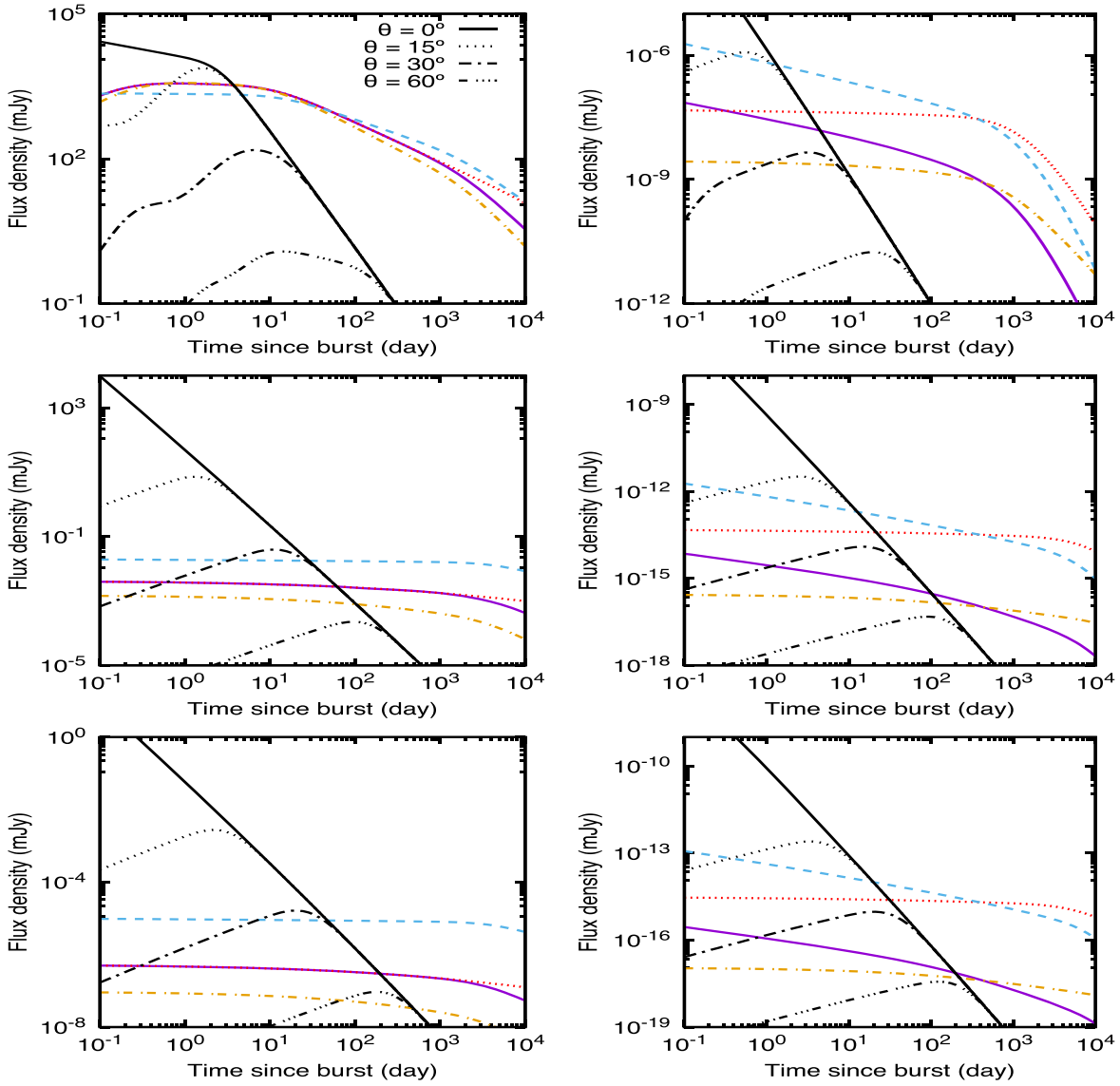

Figure 8. SSC and synchrotron light curves generated by the deceleration of nonrelativistic masses ejected in a stellar-wind medium. The left panels show the synchrotron light curves that correspond to (from top to bottom) the radio (1.6 GHz), optical (1 eV), and X-ray (1 keV) bands, and the right panels show the SSC light curves that correspond to (from top to bottom) the gamma-ray fluxes at 100 keV, 10 GeV, and 100 GeV. The solid purple line is for $\alpha = 3$ and $p = 2.6$, the dashed blue line is for $\alpha = 5$ and $p = 2.6$, the dotted–dashed yellow line is for $\alpha = 3.5$ and $p = 2.2$, and the dotted red line is for $\alpha = 3.5$ and $p = 2.8$. The following parameters are used: $\tilde{E} = 10^{51}$ erg, $A_2 = 3 \times 10^{36}$ cm^{-1}, $\epsilon_B = 10^{-2}$, $\epsilon_e = 10^{-1}$, and $d = 100$ Mpc.

6. The Nonrelativistic Ejecta Mass and the KN Afterglow in GW170817 and S190814bv

The coalescence of NS–NS and BH–NS binaries is the most natural candidate for the radiation of continuous GWs (e.g., see Metzger 2017). These coalescences are predicted to be accompanied by a KN (Li & Paczyński 1998; Rosswog 2005; Metzger et al. 2010; Kasen et al. 2013; Metzger 2017). This transient is expected to be observed in near-IR/optical/UV bands throughout a timescale of days to weeks.

All coalescences of NS–NS binaries and only a fraction of BH–NS binaries can unbind at least some extremely neutron-rich material, which can form heavy r-process nuclei. This lanthanide-bearing matter with high opacity is associated with the "red" KN located inside the tidal tail in the equatorial plane. The "blue" KN is associated with the low-opacity ejecta free of lanthanide-group elements that is located in the polar regions (Metzger & Fernández 2014; Perego et al. 2014; Wanajo et al. 2014; Miller et al. 2019). While the red KN is associated with a slow ejecta material $\beta \simeq 0.1$, the blue KN is characterized by ejection with a higher velocity $\beta \simeq 0.3$.

In the following section, we give a brief introduction of multiwavelength observations and also constrain the parameter space of the faster blue-KN afterglow in GW170817 and the KN afterglow possibly generated by the coalescence of a BH–NS system in S190814bv.

6.1. Multiwavelength Observations

6.1.1. GW170817

On 2017 August 17, a GW signal (GW170817; Abbott et al. 2017a, 2017b) together with a faint gamma-ray counterpart (GRB 170817A; Goldstein et al. 2017; Savchenko et al. 2017) and KN emission was detected (Coulter et al. 2017; Cowperthwaite et al. 2017; Smartt et al. 2017; Soares-Santos et al. 2017; Tanvir et al. 2017; Gottlieb et al. 2018), for the first

Table 2
The Latest Data Points from Chandra Afterglow Observations of GRB 170817A

δt (days)	F_X (0.3–10 keV) ($\times 10^{15}$ erg cm^{-2} s^{-1})	F_ν (1 keV) ($\times 10^{-7}$ mJy)	Γ_X
358.6	$7.75^{+2.70}_{-0.73}$	$6.77^{+2.36}_{-0.64}$	$1.69^{+0.49}_{-0.34}$
582.2	$3.25^{+0.85}_{-1.03}$	$2.76^{+0.72}_{-0.88}$	1.57
741.9	$2.21^{+0.85}_{-0.79}$	$1.88^{+0.72}_{-0.67}$	1.57
940	$1.10^{+0.60}_{-0.60}$	$0.95^{+0.52}_{-0.52}$	1.585

Note. The data points in erg cm^{-2} s^{-1} are taken from Hajela et al. (2019) and Troja et al. (2020a).

time, indicating the coalescence of a binary NS system. GRB 170817A exhibited observational evidence for extended emission in the X-ray (Troja et al. 2017b; Alexander et al. 2018; D'Avanzo et al. 2018; Margutti et al. 2018), optical (Lyman et al. 2018; Margutti et al. 2018), and radio (Abbott et al. 2017b; Dobie et al. 2018; Troja et al. 2017a; Mooley et al. 2018b) bands. About 11 hr post-merger, the optical transient coincident with the quiescent galaxy NGC 4993 at a distance of 40 Mpc ($z \approx 0.01$) was associated with the KN (AT 2017gfo; Coulter et al. 2017; Cowperthwaite et al. 2017; Smartt et al. 2017; Soares-Santos et al. 2017; Tanvir et al. 2017; Gottlieb et al. 2018).

The temporarily extended X-ray and radio emission was fitted with a simple PL function that increased steadily as $\sim t^{0.8}$ (Margutti et al. 2018; Mooley et al. 2018b), reaching its maximum value $\sim$140 days post-merger, then decreased subsequently as t^{-p} with $p \approx 2.2$. A variety of off-axis jet models (with an opening angle of $\lesssim 5°$ and a viewing angle of $\lesssim 28°$; Abbott et al. 2017a; Evans et al. 2017; Haggard et al. 2017; Sobacchi et al. 2017; Mandel 2018), including top-hat jets (Alexander et al. 2017, 2018; Troja et al. 2017b; Margutti et al. 2018; Fraija et al. 2019a, 2020), radially stratified outflows (Hotokezaka et al. 2018; Mooley et al. 2018b; Fraija et al. 2019d), and structured outflows (Kasliwal et al. 2017b; Lamb & Kobayashi 2017; Gottlieb et al. 2018; Kathirgamaraju et al. 2018; Lazzati et al. 2018; Mooley et al. 2018a; Fraija et al. 2019c), have been proposed to describe the temporarily extended electromagnetic emissions.

In order to constrain the KN afterglow, we use the data points displayed in Fraija et al. (2019c) and complemented with those presented by Fong et al. (2019) in the optical F606W filter and by Hajela et al. (2019) and Troja et al. (2020b) in the energy range of 0.3–10 keV. Table 2 shows the latest Chandra afterglow observations in units of erg cm^{-2} s^{-1} (0.3–10 keV) and mJy normalized at 1 keV. The data points in erg cm^{-2} s^{-1} are taken from Hajela et al. (2019) and Troja et al. (2020b).

6.1.2. S190814bv

On 2019 August 14 the LIGO and Virgo interferometer detected a GW signal (S190814bv; LIGO Scientific Collaboration & Virgo Collaboration 2019a, 2019b) associated with a BH–NS merger located at a distance of 267 $\pm$ 52 Mpc (Gomez et al. 2019). Immediately, S190814bv was followed up by a large observational campaign that covered a large fraction of the electromagnetic spectrum (e.g., see Dobie et al. 2019; Ackley et al. 2020; Andreoni et al. 2020; Vieira et al. 2020; Watson et al. 2020). No counts were registered in any wavelengths, and upper limits were reported.

Using the MegaCam instrument on the Canada–France–Hawaii Telescope, Ackley et al. (2020) placed optical upper limits on the presence of any counterpart and discussed the implications of the KN possibly being generated by the coalescence of the BH–NS system. They excluded a KN with a large ejecta mass of $\gtrsim 0.1 M_\odot$, and considering off-axis jet models, the authors ruled out circumstellar densities of $\gtrsim 1$ cm^{-3} for typical values of microphysical parameters. Vieira et al. (2020) reported observational constraints on the near-IR and optical with ENGRAVE (Electromagnetic Counterparts of Gravitational Wave Sources at the Very Large Telescope). They constrained the KN ejecta mass to $\lesssim 1.5 \times 10^{-2} M_\odot$ for a blue KN and to $\lesssim 4 \times 10^{-2} M_\odot$ for a red KN. Gomez et al. (2019) reported a Galaxy-targeted search for optical emission with the Magellan Baade 6.5 m telescope and ruled out the on-axis typical jet of sGRBs. Dobie et al. (2019) presented upper limits in the radio band with the Australian Square Kilometre Array Pathfinder and constrained the circumstellar density and inclination angle of the system.

In order to constrain the KN afterglow, upper limits in radio at 935 MHz (Dobie et al. 2019), in the near-IR and optical at the K_s and R filters (Ackley et al. 2020), and in X-rays at 1 keV (Evans et al. 2019) are considered.

6.2. Constraining the KN Afterglow

Figure 9 shows the multiwavelength observations of GW170817 and S190814bv at the radio, optical, and X-ray bands with the synchrotron light curves shown in Figure 1, which are generated by the deceleration of the nonrelativistic ejecta in the homogeneous-density medium. Each color of the synchrotron light curves corresponds to the set of parameter values reported in Section 3. In addition, we include the synchrotron light curves at 3 GHz. The data points with upper limits in black correspond to the observations performed for GW170817, and those with upper limits in gray correspond to S190814bv. Concerning GW170817, the upper panels show the radio observations at 3 GHz (left) and 6 GHz (right), and the lower panels show the optical observations at the F606W filter and the X-ray observations at 1 keV (right). We include the upper limits collected from S190814bv in radio at 935 MHz (top left), in the near-IR and optical at the K_s and R filters (bottom left), and in X-rays at 1 keV (bottom right).

As indicated in Section 3, the synchrotron light curves are shown for different values of p and α and the same values of A_0, ϵ_e, and ϵ_B. Therefore, any variation of these parameters will increase or decrease the intensity of the observed flux in the radio, optical, and X-ray bands. Given the multiwavelength observations of GW170817 and S190814bv, we constrain the parameter space of A_0, α, ϵ_e, and ϵ_B as a function of the velocity β. In order to compare the density parameter of the uniform-density medium A_0 found in this model with others, hereafter we use the usual notation n for A_0.

6.2.1. GW170817

Figure 10 shows the multiwavelength observations of GW170817 and the parameter space allowed with the synchrotron model presented in this work. The upper left panel shows the multiwavelength data points of GW170817 with the best-fit curves obtained with the structured jet model presented in Fraija et al. (2019c) and a possible synchrotron contribution emitted by the deceleration of the nonrelativistic

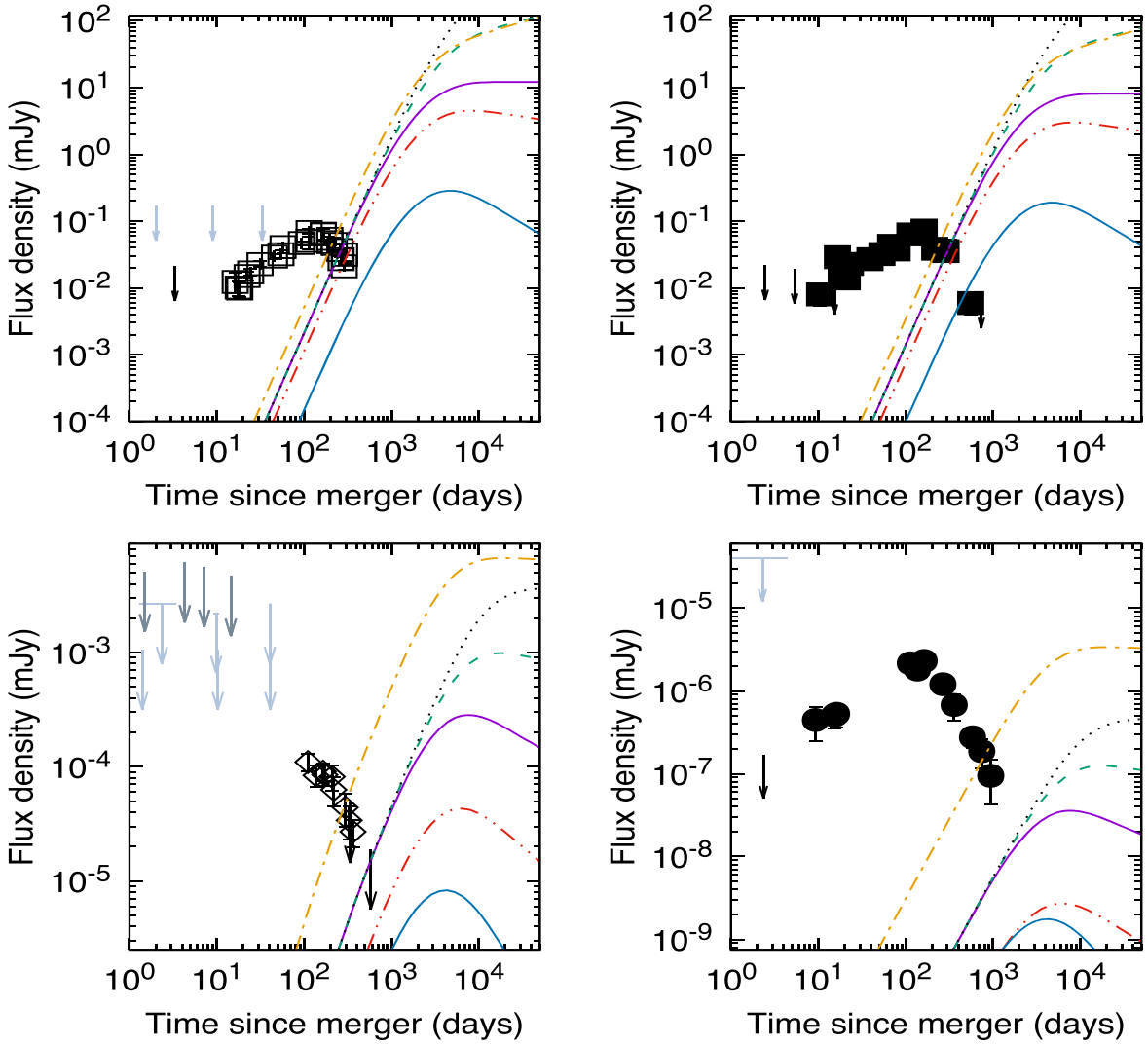

Figure 9. Multiwavelength observations and upper limits of GRB 170817A and S190814bv at the radio, optical, and X-ray bands with the synchrotron light curves generated by the deceleration of the nonrelativistic ejecta for $k = 0$ (see Figure 1). The upper panels show the radio observations at 3 GHz (left) and 6 GHz (right), and the lower panels show the observations at the F606W filter (left) and 1 keV (right). The solid curves in blue for the optical and X-ray bands are multiplied by 60 and 1.6×10^3, respectively, as illustrated in each panel. The data points of GRB 170817A are taken from Fong et al. (2019), Fraija et al. (2019c), Hajela et al. (2019), and Troja et al. (2020a), and the upper limits of S190814bv are taken from Dobie et al. (2019), Ackley et al. (2020), and Evans et al. (2019). The data conversion of the latest Chandra afterglow observations between erg cm^{-2} s^{-1} (0.3–10 keV) and mJy normalized at 1 keV is reported in Table 2.

ejecta. The light curves are exhibited in the radio (3 and 6 GHz), optical (at the F606W filter), and X-ray (1 keV) bands. The upper right panel and the lower panels show the allowed parameter space of the uniform density of the circumstellar medium (n), the velocity of the nonrelativistic ejecta (β), the index of the PL distribution (α), and the microphysical parameters (ϵ_e and ϵ_B) for the fiducial energy $\tilde{E}_K = 10^{49}$ erg (Hotokezaka & Piran 2015; Fraija et al. 2019c) and the spectral index $p = 2.15$ (Lazzati et al. 2018; Hajela et al. 2019). We use a value of the microphysical parameter $\epsilon_e = 10^{-1}$ and $\alpha = 3.0$ in the upper left panel, $\epsilon_B = 10^{-3}$ and $\alpha = 3.0$ in the lower right panel, and $\epsilon_e = 10^{-1}$ and $\epsilon_B = 10^{-3}$ in the lower left panel. The allowed parameter spaces are below the relevant colored contours and are obtained using the data points in the radio, optical, and X-ray bands as upper limits. In order to illustrate the synchrotron light curves generated by the deceleration of the nonrelativistic ejecta as shown in the upper left panel, we consider a set of values from the parameter space.

Taking into account the velocity of $\beta = 0.3$ and $\alpha = 3$, which are the reported values for the blue KN (Metzger 2019), the ranges of parameters allowed in our model ($5 \times 10^{-2} \lesssim \epsilon_e \lesssim 0.2$, $10^{-3} \lesssim \epsilon_B \lesssim 10^{-2}$, and $10^{-3} \lesssim n \lesssim 10^{-2}$ cm^{-3}) are similar to those reported in the description of multiwavelength observations by the deceleration of relativistic structured/top-hat outflows. For instance, the values $\epsilon_e = 0.15$, $\epsilon_B = 5 \times 10^{-3}$, and $n = 4 \times 10^{-3}$ cm^{-3} for $\beta \approx 0.3$ strongly agree with the values reported in Hajela et al. (2019).

6.2.2. S190814bv

Figure 11 shows the multiwavelength upper limits of S190814bv and the parameter space ruled out with the synchrotron model presented in this work. The upper left panel shows the multiwavelength upper limits and the light curves in the X-ray, optical, near-IR, and radio bands at 1 keV, the R band, the K_s band, and 943 MHz, respectively. In order to rule out the parameters n, α, β, ϵ_e, and ϵ_B, these upper limits are

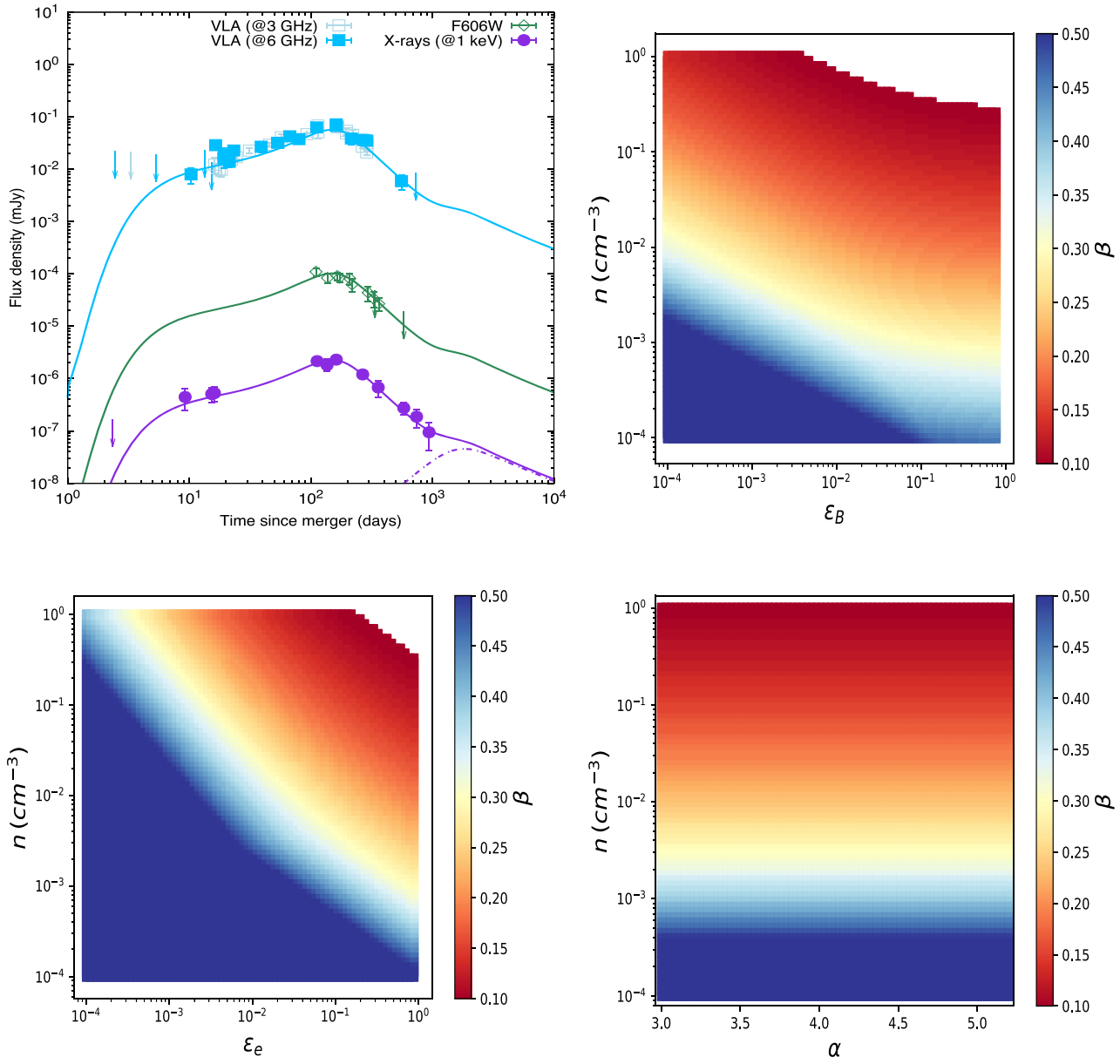

Figure 10. Upper left panel shows the multiwavelength data points of GRB 170817A with the best-fit curves obtained with the structure jet model presented in Fraija et al. (2019c) and a possible synchrotron light curve from the deceleration of the nonrelativistic ejecta. The upper right and lower panels show the allowed parameter space of the uniform density of the circumstellar medium (n), the velocity of the nonrelativistic ejecta (β), and the microphysical parameters (ϵ_e and ϵ_B) for the fiducial energy $E = 10^{49}$ erg, $\alpha = 3.0$, and the spectral index $p = 2.15$. A value of the microphysical parameter $\epsilon_e = 10^{-1}$ is used in the left panel, and $\epsilon_B = 10^{-3}$ is used in the right panel.

considered. The ruled-out regions are above the relevant colored contours. The upper right and lower panels show the parameter spaces that are ruled out in our model for the fiducial energy $\tilde{E} = 10^{50}$ erg and the spectral index $p = 2.6$. We use a value of the microphysical parameter $\epsilon_e = 10^{-1}$ and $\alpha = 3$ in the upper right panel, $\epsilon_B = 10^{-2}$ and $\alpha = 3$ in the lower left panel, and $\epsilon_e = 10^{-1}$ and $\epsilon_B = 10^{-2}$ in the lower right panel. These panels show that a uniform density $n \gtrsim 0.6\,\mathrm{cm}^{-3}$ is ruled out in our model for the parameters in the range of $3 \lesssim \alpha \lesssim 5.2$, $0.1 \lesssim \epsilon_e \lesssim 0.9$, and $10^{-2} \lesssim \epsilon_B \lesssim 0.1$ for $\beta > 0.33$. In order to illustrate the synchrotron light curves in the X-ray, optical, near-IR, and radio bands generated by the deceleration of the nonrelativistic ejecta as shown in the upper panel, we consider a set of parameters selected from the lower panels ($\beta = 0.39$, $\alpha = 3$, $\epsilon_B = 0.1$, $\epsilon_e = 0.3$, and $n = 1\,\mathrm{cm}^{-3}$). In this panel it can be observed that the predicted radio flux is above the upper limit at 37 days.

The value of the uniform-density medium ruled out in our model is consistent with the values of densities derived by Dobie et al. (2019), Ackley et al. (2020), and Gomez et al. (2019) using distinct off-axis jet models. Further observations on timescales of years post-merger are needed to derive tighter constraints and therefore to increase (decrease) the parameter space ruled out (allowed) in our model. The value allowed of the power index $\alpha = 3$ in our theoretical model agrees with the values found in numerical simulations (e.g., see Bauswein et al. 2013) and used for describing KN emission (Metzger 2017, 2019).

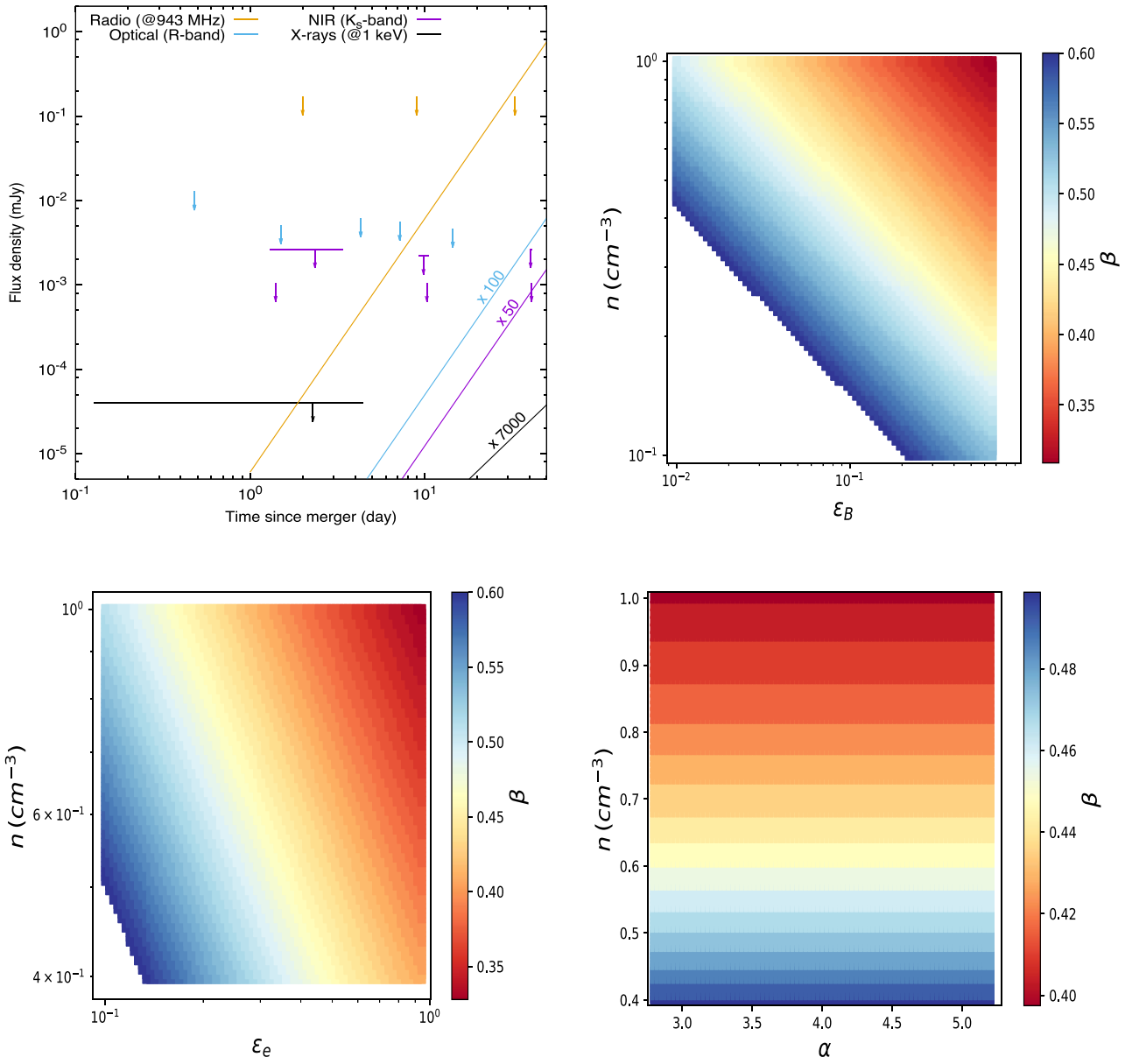

Figure 11. Upper left panel shows the multiwavelength upper limits of S190814bv and the parameter space ruled out with the synchrotron model presented in this work. The upper right and lower panels show the parameter space of the uniform density of the circumstellar medium (n), the velocity of the nonrelativistic ejecta (β), and the microphysical parameters (ϵ_e and ϵ_B) ruled out in our model for the fiducial energy $E = 10^{50}$ erg, $\alpha = 3.0$, and the spectral index $p = 2.6$. A value of the microphysical parameter $\epsilon_e = 10^{-1}$ is used in the left panel, and $\epsilon_B = 10^{-2}$ is used in the right panel.

6.3. A Diverse Range of KN Features

Disentangling the properties of KNe is an important point especially given the association of sGRBs with GWs. The detection of GRB 170817A, AT 2017gfo, and GW170817 has paved the way toward defining sGRBs as the coalescence of NS binaries. The evident KN signature in GW170817 has provided the chance to estimate the detectability of KNe in sGRBs and the variability of their features. Since sGRBs are usually discovered via detection of gamma-ray prompt emission from the relativistic jet, they are typically observed where the afterglow is brighter and thus most probably obscures the KN. This emission with its more isotropic component is easier to see at angles far away from the sGRB jet (Metzger & Berger 2012). Despite this, it has been possible to determine only four claimed KNe with different features from those of AT 2017gfo. The sGRBs associated with these claimed KNe are GRB 050709 (Jin et al. 2016), GRB 060614 (Yang et al. 2015), GRB 130603B (Berger et al. 2013; Tanvir et al. 2013), and GRB 160821B (Kasliwal et al. 2017a; Troja et al. 2019). For instance, while the KN associated with GRB 060614 is much brighter (by two or three times) than the interpolated KN model fit at the time of the observations, the KN associated with GRB 160821B is less bright than AT 2017gfo. Gompertz et al. (2018) analyzed a sample of 23 nearby ($z \leqslant 0.5$) sGRBs to compare the optical and near-IR light curves with those of AT 2017gfo. They considered short bursts—following historical classification, those with $T_{90} \leqslant 2$ s—and the class of sGRBs with extended emission (Norris & Bonnell 2006; Dainotti et al. 2010, 2016, 2017a, 2017b). This comparison enabled them to characterize diversity in terms of the brightness distribution. Gompertz et al. (2018)

found that for four sGRBs—050509B, 051210, 061201, and 080905A—a KN of the same brightness of AT 2017gfo could have been observed. For these bursts, deep 3σ upper limits, two or more times dimmer than detections of AT 2017gfo at comparable rest-frame times, seem to exclude the presence of a KN like AT 2017gfo. In each case, a KN like AT 2017gfo could have been detected if it had been present. The authors also found that the afterglows in GRBs 150424A, 140903A, and 150101B were too bright for an AT 2017gfo–like KN to be detected. Finally, they reported that the host galaxies of sGRBs 061006, 071227, and 170428A were too bright, and in six bursts there were no sufficient constraining observations regarding the presence of KNe.

Covering 14 yr of operations with Swift, Dichiara et al. (2020) presented a systematic search for sGRBs in the local universe. The authors found no events at a distance of $\lesssim$100 Mpc and four candidates located at $\lesssim$200 Mpc. They derived, in each case, constraining optical upper limits on the onset of a blue KN, implying low-mass ejecta ($\lesssim 10^{-3}\,M_{\odot}$).

The bursts that exclude the evidence of a KN similar to AT 2017gfo by several magnitudes together with the properties of previously claimed KNe in sGRBs support the hypothesis that a significant diversity exists in the properties of KNe drawn from the coalescence of compact objects. This diversity of KN features leads to a wide parameter space of velocities, PL indices, masses, microphysical parameters, and circumburst densities as discussed in this section.

Continuous energy injection by the central engine on the afterglow can produce a refreshed shock and modifies the dynamics, leading to rich radiation signatures. The problem of additional energy injection from the central engine has been studied by some authors (e.g., see Gao et al. 2013a; Troja et al. 2020b). Although this scenario is beyond the scope of the current paper, these signatures, in our model, would usually appear in timescales of weeks to hundreds of days. In a forthcoming paper, we will present a detailed analysis of a refreshed shock in the energy injection scenario.

7. Discussion and Summary

We derived, based on analytic arguments, the dynamics of deceleration of nonrelativistic ejecta in a circumstellar medium with a density profile $A_k r^{-k}$ with $k = 0$, 1, 1.5, 2, and 2.5 that covers sGRB and lGRB progenitors. While the uniform-density medium ($k = 0$) is expected in the coalescence of binary compact objects and in CC-SNe, the stratified medium ($1 \leqslant k \leqslant 2.5$) is only connected with the death of massive stars with different mass-loss evolutions at the end of their lives. Taking into account the fact that electrons are accelerated during forward shocks with a spectral index in the range $2.2 \leqslant p \leqslant 3.2$, we calculated the synchrotron and SSC light curves in the fast- and slow-cooling regimes during the coasting and deceleration phases. During the coasting phase we considered velocities in the range of $0.07 \leqslant \beta \leqslant 0.8$, and during the deceleration phase we assumed a PL velocity distribution $\propto \beta^{-\alpha}$ with $3 \leqslant \alpha \leqslant 5.2$ for a generic source located at 100 Mpc.

We showed the predicted synchrotron light curves in radio at 6 GHz, in the optical at 1 eV, and in X-rays at 1 keV for typical values of GRB afterglows. All the light curves peak on timescales of several months to a few years, similar to those observed in some SNe such as SN 2014C and SN 2016aps. However, if the ejecta mass is extremely energetic or decelerates in a very dense medium, a peak in the light curve could be expected in weeks.

We showed that when the nonrelativistic ejecta decelerates in a uniform-density medium, a flattening or rebrightening in the light curve is expected, and when this ejecta decelerates in a stratified medium, the rebrightening in the light curves is not so evident. Therefore, a flattening or rebrightening at timescales of months to years in the light curve together with GW detection would be associated with the deceleration of nonrelativistic ejecta launched during the coalescence of a binary compact object. Otherwise, we showed that an observed flux that gradually decreases on timescales of months to years could be associated with the deceleration of nonrelativistic ejecta launched during the death of a massive star with a different mass-loss evolution at the end of its life.

The coalescence of NS binaries launches significant nonrelativistic masses with different velocities that will contribute at distinct timescales, frequencies, and intensities. These ejecta masses (dynamical ejecta, cocoon material, shock breakout material, and wind ejecta) interact with the circumstellar medium, generating nonthermal emission. Shock breakout material peaks at timescales of hours to days, cocoon material peaks at timescales of weeks to months, dynamical ejecta peaks at years, and disk wind ejecta peaks at centuries. We calculated the expected gamma-ray, X-ray, optical, and radio fluxes via SSC and synchrotron emission from electrons accelerated in the forward shocks. These electromagnetic signatures at different timescales and frequencies would be similar to those detected around SNe for a uniform-density medium and also be present together with GW detections.

We showed that variations in the density parameter could be observed more easily (i) in the radio than in the X-ray light curve, (ii) in a stratified than in a uniform-density medium, and (iii) for larger values of α. Therefore, the transition phase from a stellar-wind to a uniform-density medium is more noticeable in radio than in X-ray bands.

We showed that, in the case of a failed or an off-axis GRB, the nonthermal emission generated by the deceleration of nonrelativistic ejecta could be detected at early times. In the case of an on-axis GRB, the afterglow emission originating from deceleration of the relativistic jet would have to decrease substantially so that afterglow emission from the nonrelativistic ejecta could be observed. In addition, we gave an important tool for distinguishing afterglow emission among nonrelativistic ejecta from the relativistic jet through the evolution of the synchrotron flux derived in Equations (5) and (7) for the coasting phase and in Equations (15) and (19) for the deceleration phase.

We computed the predicted SSC light curves from the deceleration of the nonrelativistic ejecta mass for a density profile with $k = 0$, 1, 1.5, 2, and 2.5. The effect of the EBL absorption modeled in Franceschini & Rodighiero (2017) was assumed. We showed that, when the nonrelativistic ejecta decelerates in a uniform-density medium, a flattening or rebrightening in the light curve is expected, and when this ejecta decelerates in a stratified medium, the rebrightening in the light curves is not so evident. Similarly, we showed that the SSC flux is less sensitive to changes in the density parameter for higher frequencies than for lower ones and is more sensitive to the density parameter for larger values of k and α.

In particular, using the multiwavelength observations and upper limits of GW170817 and S190814bv, we constrained the

parameter space of the uniform density of the circumstellar medium, the velocity of the nonrelativistic ejecta, the index of the PL distribution, and the microphysical parameters. In the case of GW170817, we found values similar to those reported in descriptions of multiwavelength observations by the deceleration of relativistic structured/top-hat outflows for typical values of KN ejecta mass $\beta \approx 0.3$ and $\alpha = 3$ (Metzger 2017, 2019). Therefore, we conclude that the KN afterglow scenario can be used to constrain the afterglow parameters of relativistic structured/top-hat outflows. In particular, the values of $\epsilon_e = 0.15$, $\epsilon_B = 5 \times 10^{-3}$, and $n = 4 \times 10^{-3}\,\mathrm{cm}^{-3}$ strongly agree with the values reported in Hajela et al. (2019). For the case of S190814bv, we found that the value of the uniform-density medium ruled out in our model is consistent with the value of density derived by Dobie et al. (2019), Ackley et al. (2020), and Gomez et al. (2019) using distinct off-axis jet models. Further observations on timescales of years post-merger are needed to derive tighter constraints and therefore to increase (decrease) the parameter space ruled out (allowed) in our model. The value allowed of the power index $\alpha = 3$ in our theoretical model agrees with the values found in numerical simulations (e.g., see Bauswein et al. 2013) and used for describing KN emission (Metzger 2017, 2019).

N.F. acknowledges financial support from UNAM-DGAPA-PAPIIT through grant IA102019. R.B.D. acknowledges support from the National Science Foundation under grant 1816694. M.G.D. acknowledges funding from the AAS Chrétien Fellowship and the MINIATURA2 grant.

Appendix
Light Curves of SSC Emission

A.1. The Free-coasting Phase

The corresponding SSC break frequencies during the free-coasting phase are given by

$$\begin{aligned} h\nu^{\rm ssc}_{\rm mm} &= \nu^{\rm ssc,0}_{\rm mm}\, g^4(p)\Big(\frac{1+z}{1.022}\Big)^{\frac{k-2}{2}} \\ &\times\ \epsilon^4_{\rm e,-1}\,\epsilon^{\frac{1}{2}}_{B,-2} A_k^{\frac{1}{2}}\beta^{\frac{18-k}{2}}_{-0.5}\, t_6^{-\frac{k}{2}} \\ h\nu^{\rm ssc}_{\rm cc} &= \nu^{\rm ssc,0}_{\rm cc}\Big(\frac{1+z}{1.022}\Big)^{\frac{6-7k}{2}}(1+Y)^{-4} \\ &\times\ \epsilon^{-\frac{7}{2}}_{B,-2}\, A_k^{-\frac{7}{2}}\beta^{\frac{7(k-2)}{2}}_{-0.5}\, t_6^{\frac{7k-8}{2}}. \end{aligned} \tag{A1}$$

For the case $\nu^{\rm syn}_{\rm a,1} \leqslant \nu^{\rm syn}_{\rm m} \leqslant \nu^{\rm syn}_{\rm c}$, the SSC break frequencies are

$$\begin{aligned} h\nu^{\rm ssc}_{\rm ma,1} &= \nu^{\rm ssc,0}_{\rm ma,1}\, g(p)\Big(\frac{1+z}{1.022}\Big)^{\frac{4(k-2)}{5}} \\ &\times\ \epsilon_{\rm e,-1}\,\epsilon^{\frac{1}{5}}_{B,-2} A_k^{\frac{4}{5}}\beta^{-\frac{4k-15}{5}}_{-0.5}\, t_6^{\frac{3-4k}{5}} \\ h\nu^{\rm ssc}_{\rm mc,1} &= \nu^{\rm ssc,0}_{\rm mc,1}\, g^2(p)\Big(\frac{1+z}{1.022}\Big)^{\frac{2-3k}{2}}(1+Y)^{-2} \\ &\times\ \epsilon^2_{\rm e,-1}\,\epsilon^{-\frac{3}{2}}_{B,-2} A_k^{-\frac{3}{2}}\beta^{\frac{3k+2}{2}}_{-0.5}\, t_6^{\frac{3k-4}{2}}. \end{aligned} \tag{A2}$$

For the case $\nu^{\rm syn}_{\rm m} \leqslant \nu^{\rm syn}_{\rm a,2} \leqslant \nu^{\rm syn}_{\rm c}$, the SSC break frequencies are

$$\begin{aligned} h\nu^{\rm ssc}_{\rm ma,2} &= \nu^{\rm ssc,0}_{\rm ma,2}\, g(p)^{\frac{2(2p+3)}{p+4}}\Big(\frac{1+z}{1.022}\Big)^{\frac{(k-2)(p+6)}{2(p+4)}} \\ &\times\ \epsilon^{\frac{2(2p+3)}{p+4}}_{\rm e,-1}\,\epsilon^{\frac{p+2}{2(p+4)}}_{B,-2} A_k^{\frac{p+6}{2(p+4)}}\beta^{\frac{18p-kp-6k+32}{2(p+4)}}_{-0.5}\, t_6^{\frac{4-kp-6k}{2(p+4)}} \\ h\nu^{\rm ssc}_{\rm mc,2} &= \nu^{\rm ssc,0}_{\rm mc,2}\, g^2(p)\Big(\frac{1+z}{1.022}\Big)^{\frac{2-3k}{2}}(1+Y)^{-2} \\ &\times\ \epsilon^2_{\rm e,-1}\,\epsilon^{-\frac{3}{2}}_{B,-2} A_k^{-\frac{3}{2}}\beta^{\frac{3k+2}{2}}_{-0.5}\, t_6^{\frac{3k-4}{2}} \\ h\nu^{\rm ssc}_{\rm ca,2} &= \nu^{\rm ssc,0}_{\rm ca,2}\, g(p)^{\frac{2(p-1)}{p+4}} \\ &\times\ \Big(\frac{1+z}{1.022}\Big)^{\frac{4-10k+2p-3kp}{2(p+4)}}(1+Y)^{-2} \\ &\times\ \epsilon^{\frac{2(p-1)}{p+4}}_{\rm e,-1}\,\epsilon^{-\frac{3p+14}{2(p+4)}}_{B,-2} A_k^{-\frac{3p+10}{2(p+4)}}\beta^{\frac{3kp+10k+2p-32}{2(p+4)}}_{-0.5}\, t_6^{\frac{10k-4p+3kp-12}{2(p+4)}}, \end{aligned} \tag{A3}$$

and for $\nu^{\rm syn}_{\rm a,3} \leqslant \nu^{\rm syn}_{\rm c} \leqslant \nu^{\rm syn}_{\rm m}$, they are

$$\begin{aligned} h\nu^{\rm ssc}_{\rm ca,3} &= \nu^{\rm ssc,0}_{\rm ca,3}\Big(\frac{1+z}{1.022}\Big)^{-\frac{k+3}{5}}(1+Y)^{-1} \\ &\times\ \epsilon^{-\frac{4}{5}}_{B,-2} A_k^{-\frac{1}{5}}\beta^{\frac{k-5}{5}}_{-0.5}\, t_6^{\frac{k-2}{5}} \\ h\nu^{\rm ssc}_{\rm cm,3} &= \nu^{\rm ssc,0}_{\rm cm,3}\, g^2(p)\Big(\frac{1+z}{1.022}\Big)^{\frac{2-3k}{2}}(1+Y)^{-2} \\ &\times\ \epsilon^2_{\rm e,-1}\,\epsilon^{-\frac{3}{2}}_{B,-2} A_k^{-\frac{3}{2}}\beta^{\frac{3k+2}{2}}_{-0.5}\, t_6^{\frac{3k-4}{2}}. \end{aligned} \tag{A4}$$

The spectral peak flux density of SSC emission $F^{\rm ssc}_{\rm max} \sim \frac{4}{3} g(p)^{-1}\sigma_{\rm T} A_k\, r^{1-k}\, F^{\rm syn}_{\rm max}$, with $\sigma_{\rm T}$ denoting the Thomson cross section, is given by

$$\begin{aligned} F^{\rm ssc}_{\nu,\rm max} &= F^{\rm ssc,0}_{\nu,\rm max}\, g(p)^{-1}\Big(\frac{1+z}{1.022}\Big)^{\frac{5k-6}{2}} \\ &\times\ \epsilon^{\frac{1}{2}}_{B,-2}\, d^{-2}_{z,26.5}\, A_k^{\frac{5}{2}}\,\beta^{\frac{5(2-k)}{2}}_{-0.5}\, t_6^{\frac{8-5k}{2}}. \end{aligned} \tag{A5}$$

The terms $\nu^{\rm ssc,0}_{\rm mm}$, $\nu^{\rm ssc,0}_{\rm cc}$, $\nu^{\rm ssc,0}_{\rm ma,1}$, $\nu^{\rm ssc,0}_{\rm mc,1}$, $\nu^{\rm ssc,0}_{\rm ma,2}$, $\nu^{\rm ssc,0}_{\rm mc,2}$, $\nu^{\rm ssc,0}_{\rm ca,2}$, $\nu^{\rm ssc,0}_{\rm ma,3}$, $\nu^{\rm ssc,0}_{\rm mc,3}$, and $F^{\rm ssc,0}_{\nu,\rm max}$ are given in Table 1 for $k = 0$, 1, 1.5, 2, and 2.5.

Using the SSC break frequencies (Equations (A1), (A2), (A3), and (A4)) and the spectral peak flux density (Equation (A5)), the SSC light curves in the fast- and slow-cooling regimes evolve as

$$F^{\rm ssc}_{\nu} \propto \begin{cases} t^{\frac{28-19k}{5}}\nu, & \nu < \nu^{\rm ssc}_{\rm ca,3}, \\ t^{\frac{16-11k}{3}}\nu^{\frac{1}{3}}, & \nu^{\rm ssc}_{\rm ca,3} < \nu < \nu^{\rm ssc}_{\rm cc}, \\ t^{\frac{8-3k}{4}}(C_{\rm cf,11} + C_{\rm cf,12}\ln[t^{\frac{8-7k}{2}}\nu])\nu^{-\frac{1}{2}}, & \nu^{\rm ssc}_{\rm cc} < \nu < \nu^{\rm ssc}_{\rm cm,3}, \\ t^{\frac{8-3k}{4}}(C_{\rm cf,21} + C_{\rm cf,22}\ln[t^{-\frac{k}{2}}\nu^{-1}])\nu^{-\frac{1}{2}}, & \nu^{\rm ssc}_{\rm cm,3} < \nu < \nu^{\rm ssc}_{\rm mm}, \\ t^{\frac{8-k(p+2)}{4}}(C_{\rm cf,31} + C_{\rm cf,32}\ln[t^{\frac{k}{2}}\nu])\nu^{-\frac{p}{2}}, & \nu^{\rm ssc}_{\rm mm} < \nu, \end{cases} \tag{A6}$$

$$F_\nu^{\rm ssc}\propto\begin{cases}t^{-\frac{9(k-2)}{5}}\nu, & \nu<\nu_{\rm ma,1}^{\rm ssc},\\ t^{\frac{12-7k}{3}}\nu^{\frac{1}{3}}, & \nu_{\rm ma,1}^{\rm ssc}<\nu<\nu_{\rm mm}^{\rm ssc},\\ t^{\frac{16-9k-kp}{4}}(C_{\rm cs1,11}+C_{\rm cs1,12}\ln[t^{\frac{k}{2}}\nu])\nu^{\frac{1-p}{2}}, & \nu_{\rm mm}^{\rm ssc}<\nu<\nu_{\rm mc,1}^{\rm ssc},\\ t^{\frac{16-9k-kp}{4}}(C_{\rm cs1,21}+C_{\rm cs1,22}\ln[t^{\frac{7k-8}{2}}\nu^{-1}])\nu^{\frac{1-p}{2}}, & \nu_{\rm mc,1}^{\rm ssc}<\nu<\nu_{\rm cc}^{\rm ssc},\\ t^{\frac{8-2k-kp}{4}}(C_{\rm cs1,31}+C_{\rm cs1,32}\ln[t^{\frac{8-7k}{2}}\nu])\nu^{-\frac{p}{2}}, & \nu_{\rm cc}^{\rm ssc}<\nu,\end{cases}\tag{A7}$$

and

$$F_\nu^{\rm ssc}\propto\begin{cases}t^{-\frac{3(k-2)(p+5)}{2(p+4)}}\nu, & \nu<\nu_{\rm ma,2}^{\rm ssc},\\ t^{\frac{16-9k-kp}{4}}(C_{\rm cs2,11}+C_{\rm cs2,12}\ln[t^{\frac{k(p+6)-4}{2(p+4)}}\nu])\nu^{\frac{1-p}{2}}, & \nu_{\rm ma,2}^{\rm ssc}<\nu<\nu_{\rm mc,2}^{\rm ssc},\\ t^{\frac{16-9k-kp}{4}}(C_{\rm cs2,21}+C_{\rm cs2,22}\ln[t^{\frac{k(2p+9)-2(p+5)}{p+4}}])\nu^{\frac{1-p}{2}}, & \nu_{\rm mc,2}^{\rm ssc}<\nu<\nu_{\rm ca,2}^{\rm ssc},\\ t^{\frac{16-9k-kp}{4}}(C_{\rm cs2,31}+C_{\rm cs2,32}\ln[t^{\frac{7k-8}{2}}\nu^{-1}])\nu^{\frac{1-p}{2}}, & \nu_{\rm ca,2}^{\rm ssc}<\nu<\nu_{\rm cc}^{\rm ssc},\\ t^{\frac{8-2k-kp}{4}}(C_{\rm cs2,41}+C_{\rm cs2,42}\ln[t^{\frac{8-7k}{2}}\nu])\nu^{-\frac{p}{2}}, & \nu_{\rm cc}^{\rm ssc}<\nu.\end{cases}\tag{A8}$$

The parameters $C_{\rm cf}$, $C_{\rm cs,1}$, and $C_{\rm cs,2}$ do not evolve with time.

A.2. The Deceleration Phase

The PL indices m_{ij} for $i,\ j=1,\ 2,$ and 3 are $m_{11}=-\frac{55+8\alpha-k(21+4\alpha)}{5(\alpha+5-k)}$, $m_{12}=\frac{-2p(\alpha-10)+kp(\alpha-6)+6k(\alpha+4)-12(\alpha+5)}{2(p+4)(\alpha+5-k)}$, $m_{13}=\frac{k(16+9\alpha)-13\alpha-20}{5(\alpha+5-k)}$, $m_{21}=\frac{3\alpha-16k+30-4k\alpha}{5(\alpha+5-k)}$, $m_{22}=\frac{4\alpha-6k\alpha-\alpha kp+8kp-30p-16k+20}{2(p+4)(\alpha+5-k)}$, and $m_{23}=\frac{8\alpha-9k\alpha-11k-5}{5(\alpha+5-k)}$.

The corresponding SSC break frequencies during the deceleration phase are given by

$$\begin{aligned}h\nu_{\rm mm}^{\rm ssc}&=\nu_{\rm mm}^{\rm ssc,0}\Big(\frac{1+z}{1.022}\Big)^{\frac{44+k(\alpha-14)-2\alpha}{2(\alpha+5-k)}}\ g(p)^4\epsilon_{\rm e,-1}^4\ \epsilon_{B,-2}^{\frac{1}{2}}\\&\times A_k^{\frac{\alpha-13}{2(\alpha+5-k)}}\ \tilde{E}_{51}^{\frac{18-k}{2(\alpha+5-k)}}\ t_7^{-\frac{54+k(\alpha-16)}{2(\alpha+5-k)}}\\ h\nu_{\rm cc}^{\rm ssc}&=\nu_{\rm cc}^{\rm ssc,0}\Big(\frac{1+z}{1.022}\Big)^{\frac{6\alpha-7k\alpha-6k-12}{2(\alpha+5-k)}}\ \epsilon_{B,-2}^{-\frac{7}{2}}\ (1+Y)^{-4}\\&\times A_k^{-\frac{7(\alpha+3)}{2(\alpha+5-k)}}\ \tilde{E}_{51}^{\frac{7(k-2)}{2(\alpha+5-k)}}\ t_7^{\frac{2+8k-8\alpha+7k\alpha}{2(\alpha+5-k)}}.\end{aligned}\tag{A9}$$

For the case $\nu_{\rm a,1}^{\rm syn}\leqslant\nu_{\rm m}^{\rm syn}\leqslant\nu_{\rm c}^{\rm syn}$, the SSC break frequencies are

$$\begin{aligned}h\nu_{\rm ma,1}^{\rm ssc}&=\nu_{\rm ma,1}^{\rm ssc,0}\ g(p)\Big(\frac{1+z}{1.022}\Big)^{\frac{5+k-8\alpha+4k\alpha}{5(\alpha+5-k)}}\epsilon_{\rm e,-1}\ \epsilon_{B,-2}^{\frac{1}{5}}\\&\times A_k^{\frac{4\alpha+5}{5(\alpha+5-k)}}\tilde{E}_{51}^{\frac{15-4k}{5(\alpha+5-k)}}\ t_7^{\frac{3\alpha-30+4k(1-\alpha)}{5(\alpha+5-k)}}\\ h\nu_{\rm mc,1}^{\rm ssc}&=\nu_{\rm mc,1}^{\rm ssc,0}\ g^2(p)\Big(\frac{1+z}{1.022}\Big)^{\frac{16-10k+2\alpha-3k\alpha}{2(\alpha+5-k)}}(1+Y)^{-2}\\&\times\ \epsilon_{\rm e,-1}^2\ \epsilon_{B,-2}^{-\frac{3}{2}}A_k^{-\frac{3\alpha+17}{2(\alpha+5-k)}}\tilde{E}_{51}^{\frac{3k+2}{2(\alpha+5-k)}}\ t_7^{-\frac{26+4\alpha-3k(\alpha+4)}{2(\alpha+5-k)}}.\end{aligned}\tag{A10}$$

For the case $\nu_{\rm m}^{\rm syn}\leqslant\nu_{\rm a,2}^{\rm syn}\leqslant\nu_{\rm c}^{\rm syn}$, the SSC break frequencies are

$$\begin{aligned}h\nu_{\rm ma,2}^{\rm ssc}&=\nu_{\rm ma,2}^{\rm ssc,0}\ g(p)^{\frac{2(2p+3)}{p+4}}\Big(\frac{1+z}{1.022}\Big)^{\frac{36+44p-12\alpha-2p\alpha+k(6\alpha-8+p(\alpha-14))}{2(p+4)(\alpha+5-k)}}\\&\times\ \epsilon_{\rm e,-1}^{\frac{2(2p+3)}{p+4}}\ \epsilon_{B,-2}^{\frac{p+2}{2(p+4)}}A_k^{\frac{6\alpha-2+p(\alpha-13)}{2(p+4)(\alpha+5-k)}}\\&\times\ \tilde{E}_{51}^{-\frac{k(p+6)-2(9p+16)}{2(p+4)(\alpha+5-k)}}\ t_7^{-\frac{76+54p-4\alpha+k(6\alpha-16+p(\alpha-16))}{2(p+4)(\alpha+5-k)}}\\ h\nu_{\rm mc,2}^{\rm ssc}&=\nu_{\rm mc,2}^{\rm ssc,0}\ g^2(p)\Big(\frac{1+z}{1.022}\Big)^{\frac{16-10k+2\alpha-3k\alpha}{2(\alpha+5-k)}}(1+Y)^{-2}\\&\times\ \epsilon_{\rm e,-1}^2\ \epsilon_{B,-2}^{-\frac{3}{2}}A_k^{-\frac{17+3\alpha}{2(\alpha+5-k)}}\tilde{E}_{51}^{\frac{3k+2}{2(\alpha+5-k)}}\ t_7^{-\frac{26+4\alpha-3k(\alpha+4)}{2(\alpha+5-k)}}\\ h\nu_{\rm ca,2}^{\rm ssc}&=\nu_{\rm ca,2}^{\rm ssc,0}\ g(p)^{\frac{2(p-1)}{p+4}}\Big(\frac{1+z}{1.022}\Big)^{\frac{2(2(\alpha-19)+p(\alpha+8))-k(10\alpha-8+p(3\alpha+10))}{2(p+4)(\alpha+5-k)}}\\&\times\ (1+Y)^{-2}\epsilon_{\rm e,-1}^{\frac{2(p-1)}{p+4}}\ \epsilon_{B,-2}^{-\frac{3p+14}{2(p+4)}}A_k^{-\frac{18+17p+10\alpha+3p\alpha}{2(p+4)(\alpha+5-k)}}\\&\times\ \tilde{E}_{51}^{\frac{10k-32+2p+3kp}{2(p+4)(\alpha+5-k)}}\ t_7^{\frac{36+2(5k-6)\alpha+p(3k(\alpha+4)-26-4\alpha)}{2(p+4)(\alpha+5-k)}}\end{aligned}\tag{A11}$$

and for $\nu_{\rm a,3}^{\rm syn}\leqslant\nu_{\rm c}^{\rm syn}\leqslant\nu_{\rm m}^{\rm syn}$, they are

$$\begin{aligned}h\nu_{\rm ca,3}^{\rm ssc}&=\nu_{\rm ca,3}^{\rm ssc,0}\Big(\frac{1+z}{1.022}\Big)^{-\frac{k(\alpha-6)+3(\alpha+10)}{5(\alpha+5-k)}}(1+Y)^{-1}\ \epsilon_{B,-2}^{\frac{4}{5}}\\&\times\ A_k^{-\frac{\alpha}{5(\alpha+5-k)}}\tilde{E}_{51}^{\frac{k-5}{5(\alpha+5-k)}}\ t_7^{\frac{5-k-2\alpha+k\alpha}{5(\alpha+5-k)}}\\ h\nu_{\rm cm,3}^{\rm ssc}&=\nu_{\rm cm,3}^{\rm ssc,0}\ g^2(p)\Big(\frac{1+z}{1.022}\Big)^{\frac{16-10k+2\alpha-3k\alpha}{2(\alpha+5-k)}}(1+Y)^{-2}\ \epsilon_{\rm e,-1}^2\epsilon_{B,-2}^{-\frac{3}{2}}\\&\times\ A_k^{-\frac{3\alpha+17}{2(\alpha+5-k)}}\tilde{E}_{51}^{\frac{3k+2}{2(\alpha+5-k)}}\ t_7^{\frac{3k(\alpha+4)-26-4\alpha}{2(\alpha+5-k)}}.\end{aligned}\tag{A12}$$

The terms $\nu_{\rm mm}^{\rm ssc,0}$, $\nu_{\rm cc}^{\rm ssc,0}$, $\nu_{\rm ma,1}^{\rm ssc,0}$, $\nu_{\rm mc,1}^{\rm ssc,0}$, $\nu_{\rm ma,2}^{\rm ssc,0}$, $\nu_{\rm mc,2}^{\rm ssc,0}$, $\nu_{\rm ca,2}^{\rm ssc,0}$, $\nu_{\rm ma,3}^{\rm ssc,0}$, $\nu_{\rm mc,3}^{\rm ssc,0}$, and $F_{\nu,\rm max}^{\rm ssc,0}$ are given in Table 1 for $k=0$, 1, 1.5, 2, and 2.5.

The spectral peak flux density of SSC emission is

$$F^{\rm ssc}_{\nu,\rm max} = F^{\rm ssc,0}_{\nu,\rm max}\; g(p)^{-1}\Big(\frac{1+z}{1.022}\Big)^{\frac{6k-6\alpha+5k\alpha}{2(\alpha+5-k)}}\; \epsilon_{\tilde{B},-2}^{\frac{1}{2}}\; d_{z,26.5}^{-2} \times A_k^{\frac{5(\alpha+3)}{2(\alpha+5-k)}}\; \tilde{E}_{51}^{\frac{5(2-k)}{2(\alpha+5-k)}}\; t_7^{\frac{10-8k+8\alpha-5k\alpha}{2(\alpha+5-k)}}. \quad \text{(A13)}$$

Using the SSC break frequencies (Equations (A9), (A10), (A11), and (A12)) and the spectral peak flux density (Equation (A13)), the SSC light curves in the fast- and slow-cooling regimes are

$$F^{\rm ssc}_{\nu} \propto \begin{cases} t^{\frac{20-26k+28\alpha-19k\alpha}{5(\alpha+5-k)}}\nu, & \nu < \nu^{\rm ssc}_{\rm ca,3}, \\ t^{\frac{14-16k+16\alpha-11k\alpha}{3(\alpha+5-k)}}\nu^{\frac{1}{3}}, & \nu^{\rm ssc}_{\rm ca,3} < \nu < \nu^{\rm ssc}_{\rm cc}, \\ t^{\frac{22-8k+8\alpha-3k\alpha}{4(\alpha+5-k)}}(C_{\rm df,11} + C_{\rm df,12}\ln[t^{\frac{8\alpha-2-k(8+7\alpha)}{2(\alpha+5-k)}}\nu])\nu^{-\frac{1}{2}}, & \nu^{\rm ssc}_{\rm cc} < \nu < \nu^{\rm ssc}_{\rm cm,3}, \\ t^{\frac{22-8k+8\alpha-3k\alpha}{4(\alpha+5-k)}}(C_{\rm df,21} + C_{\rm df,22}\ln[t^{-\frac{54+k(\alpha-16)}{2(\alpha+5-k)}}\nu^{-1}])\nu^{-\frac{1}{2}}, & \nu^{\rm ssc}_{\rm cm,3} < \nu < \nu^{\rm ssc}_{\rm mm}, \\ t^{\frac{76-54p-kp(\alpha-16)+8\alpha-2k(\alpha+12)}{4(\alpha+5-k)}}(C_{\rm df,31} + C_{\rm df,32}\ln[t^{\frac{54+k(\alpha-16)}{2(\alpha+5-k)}}\nu])\nu^{-\frac{p}{2}}, & \nu^{\rm ssc}_{\rm mm} < \nu, \end{cases} \quad \text{(A14)}$$

$$F^{\rm ssc}_{\nu} \propto \begin{cases} t^{\frac{9(2(\alpha+5)-k(\alpha+4))}{5(\alpha+5-k)}}\nu, & \nu < \nu^{\rm ssc}_{\rm ma,1}, \\ t^{\frac{42-20k+12\alpha-7k\alpha}{3(\alpha+5-k)}}\nu^{\frac{1}{3}}, & \nu^{\rm ssc}_{\rm ma,1} < \nu < \nu^{\rm ssc}_{\rm mm}, \\ t^{\frac{74-54p+16\alpha-k(32+p(\alpha-16)+9\alpha)}{4(\alpha+5-k)}}(C_{\rm ds1,11} + C_{\rm ds1,12}\ln[t^{\frac{54+k(\alpha-16)}{2(\alpha+5-k)}}\nu])\nu^{\frac{1-p}{2}}, & \nu^{\rm ssc}_{\rm mm} < \nu < \nu^{\rm ssc}_{\rm mc,1}, \\ t^{\frac{74-54p+16\alpha-k(32+p(\alpha-16)+9\alpha)}{4(\alpha+5-k)}}(C_{\rm ds1,21} + C_{\rm ds1,22}\ln[t^{\frac{2+8k-8\alpha+7k\alpha}{2(\alpha+5-k)}}\nu^{-1}])\nu^{\frac{1-p}{2}}, & \nu^{\rm ssc}_{\rm mc,1} < \nu < \nu^{\rm ssc}_{\rm cc}, \\ t^{\frac{76-54p-kp(\alpha-16)+8\alpha-2k(\alpha+12)}{4(\alpha+5-k)}}(C_{\rm ds1,31} + C_{\rm ds1,32}\ln[t^{\frac{8\alpha-2-k(7\alpha+8)}{2(\alpha+5-k)}}\nu])\nu^{-\frac{p}{2}}, & \nu^{\rm ssc}_{\rm cc} < \nu, \end{cases} \quad \text{(A15)}$$

and

$$F^{\rm ssc}_{\nu} \propto \begin{cases} t^{\frac{6(31+p(\alpha-1)+5\alpha)-3k(24+\alpha(p+5))}{2(p+4)(\alpha+5-k)}}\nu, & \nu < \nu^{\rm ssc}_{\rm ma,2}, \\ t^{\frac{74-54p+16\alpha-k(32+p(\alpha-16)+9\alpha)}{4(\alpha+5-k)}}(C_{\rm ds2,11} + C_{\rm ds2,12}\ln[t^{\frac{76+54p-4\alpha+k(6\alpha-16+p(\alpha-16))}{2(p+4)(\alpha+5-k)}}\nu])\nu^{\frac{1-p}{2}}, & \nu^{\rm ssc}_{\rm ma,2} < \nu < \nu^{\rm ssc}_{\rm mc,2}, \\ t^{\frac{74-54p+16\alpha-k(32+p(\alpha-16)+9\alpha)}{4(\alpha+5-k)}}(C_{\rm ds2,21} + C_{\rm ds2,22}\ln[t^{\frac{k(16+2p(\alpha-1)+9\alpha)-2(7+p(\alpha-7)+5\alpha)}{(p+4)(\alpha+5-k)}}])\nu^{\frac{1-p}{2}}, & \nu^{\rm ssc}_{\rm mc,2} < \nu < \nu^{\rm ssc}_{\rm ca,2}, \\ t^{\frac{74-54p+16\alpha-k(32+p(\alpha-16)+9\alpha)}{4(\alpha+5-k)}}(C_{\rm ds2,31} + C_{\rm ds2,32}\ln[t^{\frac{2+8k-8\alpha+7k\alpha}{2(\alpha+5-k)}}\nu^{-1}])\nu^{\frac{1-p}{2}}, & \nu^{\rm ssc}_{\rm ca,2} < \nu < \nu^{\rm ssc}_{\rm cc}, \\ t^{\frac{76-54p-kp(\alpha-16)+8\alpha-2k(\alpha+12)}{4(\alpha+5-k)}}(C_{\rm ds2,41} + C_{\rm ds2,42}\ln[t^{\frac{8\alpha-2-k(7\alpha+8)}{2(\alpha+5-k)}}\nu])\nu^{-\frac{p}{2}}, & \nu^{\rm ssc}_{\rm cc} < \nu. \end{cases} \quad \text{(A16)}$$

The parameters $C_{\rm df}$, $C_{\rm ds,1}$, and $C_{\rm ds,2}$ do not evolve with time.

ORCID iDs

N. Fraija https://orcid.org/0000-0002-0173-6453
M. G. Dainotti https://orcid.org/0000-0003-4442-8546
S. Dichiara https://orcid.org/0000-0001-6849-1270

References

Abbott, B. P., Abbott, R., Abbott, T. D., et al. 2017a, PhRvL, 119, 161101
Abbott, B. P., Abbott, R., Abbott, T. D., et al. 2017b, ApJL, 848, L12
Ackley, K., Amati, L., Barbieri, C., et al. 2020, A&A, 643, A113
Alexander, K. D., Berger, E., Fong, W., et al. 2017, ApJL, 848, L21
Alexander, K. D., Margutti, R., Blanchard, P. K., et al. 2018, ApJL, 863, L18
Ando, S., & Beacom, J. F. 2005, PhRvL, 95, 061103
Andreoni, I., Goldstein, D. A., Kasliwal, M. M., et al. 2020, ApJ, 890, 131
Arcavi, I., Hosseinzadeh, G., Howell, D. A., et al. 2017, Natur, 551, 64
Barniol Duran, R., & Giannios, D. 2015, MNRAS, 454, 1711
Barniol Duran, R., Nakar, E., Piran, T., & Sari, R. 2015, MNRAS, 448, 417
Barthelmy, S. D., Cannizzo, J. K., Gehrels, N., et al. 2005, ApJL, 635, L133
Bauswein, A., Goriely, S., & Janka, H. T. 2013, ApJ, 773, 78
Beniamini, P., Granot, J., & Gill, R. 2020, MNRAS, 493, 3521
Berger, E., Fong, W., & Chornock, R. 2013, ApJL, 774, L23
Björnsson, C.-I., & Fransson, C. 2004, ApJ, 605, 823
Blandford, R. D., & McKee, C. F. 1976, PhFl, 19, 1130
Blondin, J. M., Lundqvist, P., & Chevalier, R. A. 1996, ApJ, 472, 257
Bloom, J. S., Kulkarni, S. R., Djorgovski, S. G., et al. 1999, Natur, 401, 453
Bromberg, O., Nakar, E., & Piran, T. 2011, ApJL, 739, L55
Cano, Z., Wang, S.-Q., Dai, Z.-G., & Wu, X.-F. 2017, AdAst, 2017, 8929054
Chevalier, R. A. 1982, ApJ, 258, 790
Chevalier, R. A. 1984, ApJL, 285, L63
Chevalier, R. A., & Fransson, C. 2006, ApJ, 651, 381
Chevalier, R. A., Fransson, C., & Nymark, T. K. 2006, ApJ, 641, 1029
Chevalier, R. A., & Irwin, C. M. 2011, ApJL, 729, L6
Coulter, D. A., Foley, R. J., Kilpatrick, C. D., et al. 2017, Sci, 358, 1556
Cowperthwaite, P. S., Berger, E., Villar, V. A., et al. 2017, ApJL, 848, L17
Dai, Z. G., & Lu, T. 1999, ApJL, 519, L155
Dainotti, M. G., Hernandez, X., Postnikov, S., et al. 2017a, ApJ, 848, 88
Dainotti, M. G., Nagataki, S., Maeda, K., Postnikov, S., & Pian, E. 2017b, A&A, 600, A98
Dainotti, M. G., Postnikov, S., Hernandez, X., & Ostrowski, M. 2016, ApJL, 825, L20
Dainotti, M. G., Willingale, R., Capozziello, S., Fabrizio Cardone, V., & Ostrowski, M. 2010, ApJL, 722, L215
D'Avanzo, P., Campana, S., Salafia, O. S., et al. 2018, A&A, 613, L1
Davies, M. B., Benz, W., Piran, T., & Thielemann, F. K. 1994, ApJ, 431, 742
Dessart, L., Ott, C. D., Burrows, A., Rosswog, S., & Livne, E. 2009, ApJ, 690, 1681
Dichiara, S., Troja, E., O'Connor, B., et al. 2020, MNRAS, 492, 5011
Dobie, D., Kaplan, D. L., Murphy, T., et al. 2018, ApJL, 858, L15
Dobie, D., Stewart, A., Murphy, T., et al. 2019, ApJL, 887, L13
Evans, P. A., Cenko, S. B., Kennea, J. A., et al. 2017, Sci, 358, 1565
Evans, P. A., Kennea, J. A., Tohuvavohu, A., et al. 2019, GCN, 25400, 1
Fernández, R., Kasen, D., Metzger, B. D., & Quataert, E. 2015, MNRAS, 446, 750
Fong, W., Blanchard, P. K., Alexander, K. D., et al. 2019, ApJL, 883, L1
Fong, W., Metzger, B. D., Berger, E., & Özel, F. 2016, ApJ, 831, 141
Fraija, N. 2014, MNRAS, 437, 2187
Fraija, N., De Colle, F., Veres, P., et al. 2019a, ApJ, 871, 123
Fraija, N., De Colle, F., Veres, P., et al. 2020, ApJ, 896, 25
Fraija, N., Dichiara, S., Pedreira, A. C. C. d. E. S., et al. 2019b, ApJL, 879, L26
Fraija, N., Lopez-Camara, D., Pedreira, A. C. C. d. E. S., et al. 2019c, ApJ, 884, 71
Fraija, N., Pedreira, A. C. C. d. E. S., & Veres, P. 2019d, ApJ, 871, 200
Fraija, N., Veres, P., Zhang, B. B., et al. 2017, ApJ, 848, 15
Franceschini, A., & Rodighiero, G. 2017, A&A, 603, A34
Galama, T. J., Vreeswijk, P. M., van Paradijs, J., et al. 1998, Natur, 395, 670
Gal-Yam, A. 2017, Handbook of Supernovae (Cham: Springer), 195
Gao, H., Ding, X., Wu, X.-F., Zhang, B., & Dai, Z.-G. 2013a, ApJ, 771, 86
Gao, H., Lei, W.-H., Wu, X.-F., & Zhang, B. 2013b, MNRAS, 435, 2520
Gao, H., Wang, X.-G., Mészáros, P., & Zhang, B. 2015, ApJ, 810, 160
Geng, J.-J., Zhang, B., Kölligan, A., Kuiper, R., & Huang, Y.-F. 2019, ApJL, 877, L40
Giblin, T. W., van Paradijs, J., Kouveliotou, C., et al. 1999, ApJL, 524, L47
Goldstein, A., Veres, P., Burns, E., et al. 2017, ApJL, 848, L14
Gomez, S., Hosseinzadeh, G., Cowperthwaite, P. S., et al. 2019, ApJL, 884, L55
Gompertz, B. P., Levan, A. J., Tanvir, N. R., et al. 2018, ApJ, 860, 62
Goriely, S., Bauswein, A., & Janka, H.-T. 2011, ApJL, 738, L32
Gottlieb, O., Nakar, E., & Piran, T. 2018, MNRAS, 473, 576
Grossman, D., Korobkin, O., Rosswog, S., & Piran, T. 2014, MNRAS, 439, 757
Haggard, D., Nynka, M., Ruan, J. J., et al. 2017, ApJL, 848, L25
Hajela, A., Margutti, R., Alexander, K. D., et al. 2019, ApJL, 886, L17
Horesh, A., Kulkarni, S. R., Corsi, A., et al. 2013, ApJ, 778, 63
Hotokezaka, K., Kiuchi, K., Shibata, M., Nakar, E., & Piran, T. 2018, ApJ, 867, 95
Hotokezaka, K., Kyutoku, K., Tanaka, M., et al. 2013, ApJL, 778, L16
Hotokezaka, K., & Piran, T. 2015, MNRAS, 450, 1430
Huang, Y. F., & Cheng, K. S. 2003, MNRAS, 341, 263
Huang, Y. F., Dai, Z. G., & Lu, T. 1998, A&A, 336, L69
Huang, Y. F., Dai, Z. G., & Lu, T. 1999, MNRAS, 309, 513
Izzo, L., Auchettl, K., Hjorth, J., et al. 2020, A&A, 639, L11
Izzo, L., de Ugarte Postigo, A., Maeda, K., et al. 2019, Natur, 565, 324
Jin, Z.-P., Hotokezaka, K., Li, X., et al. 2016, NatCo, 7, 12898
Jin, Z. P., Xu, D., Covino, S., et al. 2009, MNRAS, 400, 1829
Kamble, A., Resmi, L., & Misra, K. 2007, ApJL, 664, L5
Kasen, D., Badnell, N. R., & Barnes, J. 2013, ApJ, 774, 25
Kasliwal, M. M., Korobkin, O., Lau, R. M., Wollaeger, R., & Fryer, C. L. 2017a, ApJL, 843, L34
Kasliwal, M. M., Nakar, E., Singer, L. P., et al. 2017b, Sci, 358, 1559
Kathirgamaraju, A., Barniol Duran, R., & Giannios, D. 2016, MNRAS, 461, 1568
Kathirgamaraju, A., Barniol Duran, R., & Giannios, D. 2018, MNRAS, 473, L121
Kathirgamaraju, A., Giannios, D., & Beniamini, P. 2019, MNRAS, 487, 3914
Kotak, R., Meikle, W. P. S., Adamson, A., & Leggett, S. K. 2004, MNRAS, 354, L13
Kouveliotou, C., Meegan, C. A., Fishman, G. J., et al. 1993, ApJL, 413, L101
Kulkarni, S. R., Frail, D. A., Wieringa, M. H., et al. 1998, Natur, 395, 663
Kyutoku, K., Ioka, K., & Shibata, M. 2014, MNRAS, 437, L6
Lamb, G. P., & Kobayashi, S. 2017, MNRAS, 472, 4953
Lazzati, D., López-Cámara, D., Cantiello, M., et al. 2017, ApJL, 848, L6
Lazzati, D., Morsony, B. J., Blackwell, C. H., & Begelman, M. C. 2012, ApJ, 750, 68
Lazzati, D., Perna, R., Morsony, B. J., et al. 2018, PhRvL, 120, 241103
Li, L.-X., & Paczyński, B. 1998, ApJL, 507, L59
Liang, E.-W., Li, L., Gao, H., et al. 2013, ApJ, 774, 13
LIGO Scientific Collaboration & Virgo Collaboration 2019a, GCN, 25324, 1
LIGO Scientific Collaboration & Virgo Collaboration 2019b, GCN, 25333, 1
Liu, L.-D., Gao, H., & Zhang, B. 2020, ApJ, 890, 102
Livio, M., & Waxman, E. 2000, ApJ, 538, 187
Lyman, J. D., Lamb, G. P., Levan, A. J., et al. 2018, NatAs, 2, 751
MacFadyen, A. I., Woosley, S. E., & Heger, A. 2001, ApJ, 550, 410
Mandel, I. 2018, ApJL, 853, L12
Margalit, B., & Piran, T. 2020, MNRAS, 495, 4981
Margutti, R., Alexander, K. D., Xie, X., et al. 2018, ApJL, 856, L18
Margutti, R., Kamble, A., Milisavljevic, D., et al. 2017, ApJ, 835, 140
Margutti, R., Milisavljevic, D., Soderberg, A. M., et al. 2014, ApJ, 797, 107
Margutti, R., Soderberg, A. M., Chomiuk, L., et al. 2012, ApJ, 751, 134
Margutti, R., Soderberg, A. M., Wieringa, M. H., et al. 2013, ApJ, 778, 18
Mészáros, P., & Waxman, E. 2001, PhRvL, 87, 171102
Metzger, B. D. 2017, LRR, 20, 3
Metzger, B. D. 2019, LRR, 23, 1
Metzger, B. D., Bauswein, A., Goriely, S., & Kasen, D. 2015, MNRAS, 446, 1115
Metzger, B. D., & Berger, E. 2012, ApJ, 746, 48
Metzger, B. D., & Bower, G. C. 2014, MNRAS, 437, 1821
Metzger, B. D., & Fernández, R. 2014, MNRAS, 441, 3444
Metzger, B. D., Martínez-Pinedo, G., Darbha, S., et al. 2010, MNRAS, 406, 2650
Metzger, B. D., Quataert, E., & Thompson, T. A. 2008, MNRAS, 385, 1455
Miller, J. M., Ryan, B. R., Dolence, J. C., et al. 2019, PhRvD, 100, 023008
Modjaz, M., Bianco, F. B., Siwek, M., et al. 2020, ApJ, 892, 153
Mooley, K. P., Deller, A. T., Gottlieb, O., et al. 2018a, Natur, 561, 355
Mooley, K. P., Nakar, E., Hotokezaka, K., et al. 2018b, Natur, 554, 207
Moriya, T. J., & Tominaga, N. 2012, ApJ, 747, 118
Murguia-Berthier, A., Montes, G., Ramirez-Ruiz, E., De Colle, F., & Lee, W. H. 2014, ApJL, 788, L8

Nagakura, H., Hotokezaka, K., Sekiguchi, Y., Shibata, M., & Ioka, K. 2014, ApJL, 784, L28
Nakar, E., & Piran, T. 2017, ApJ, 834, 28
Nicholl, M., Berger, E., Kasen, D., et al. 2017, ApJL, 848, L18
Nicholl, M., Blanchard, P. K., Berger, E., et al. 2020, NatAs, 4, 893
Norris, J. P., & Bonnell, J. T. 2006, ApJ, 643, 266
Panaitescu, A., & Kumar, P. 2000, ApJ, 543, 66
Perego, A., Rosswog, S., Cabezón, R. M., et al. 2014, MNRAS, 443, 3134
Piran, T., Nakar, E., & Rosswog, S. 2013, MNRAS, 430, 2121
Planck Collaboration, Ade, P. A. R., Aghanim, N., et al. 2016, A&A, 594, A13
Popham, R., Woosley, S. E., & Fryer, C. 1999, ApJ, 518, 356
Ramirez-Ruiz, E., García-Segura, G., Salmonson, J. D., & Pérez-Rendón, B. 2005, ApJ, 631, 435
Rosswog, S. 2005, ApJ, 634, 1202
Rosswog, S., Korobkin, O., Arcones, A., Thielemann, F. K., & Piran, T. 2014, MNRAS, 439, 744
Rosswog, S., Liebendörfer, M., Thielemann, F. K., et al. 1999, A&A, 341, 499
Ruffert, M., Janka, H. T., Takahashi, K., & Schaefer, G. 1997, A&A, 319, 122
Sari, R., & Esin, A. A. 2001, ApJ, 548, 787
Sari, R., & Mészáros, P. 2000, ApJL, 535, L33
Savchenko, V., Ferrigno, C., Kuulkers, E., et al. 2017, ApJL, 848, L15
Schroeder, G., Margalit, B., Fong, W.-f., et al. 2020, ApJ, 902, 82
Shibata, M., & Taniguchi, K. 2006, PhRvD, 73, 064027
Siegel, D. M., & Metzger, B. D. 2017, PhRvL, 119, 231102
Sironi, L., & Giannios, D. 2013, ApJ, 778, 107
Smartt, S. J., Chen, T. W., Jerkstrand, A., et al. 2017, Natur, 551, 75
Soares-Santos, M., Holz, D. E., Annis, J., et al. 2017, ApJL, 848, L16
Sobacchi, E., Granot, J., Bromberg, O., & Sormani, M. C. 2017, MNRAS, 472, 616
Soderberg, A. M., Chevalier, R. A., Kulkarni, S. R., & Frail, D. A. 2006, ApJ, 651, 1005
Surman, R., McLaughlin, G. C., Ruffert, M., Janka, H. T., & Hix, W. R. 2008, ApJL, 679, L117
Tan, J. C., Matzner, C. D., & McKee, C. F. 2001, ApJ, 551, 946
Tanvir, N. R., Levan, A. J., Fruchter, A. S., et al. 2013, Natur, 500, 547
Tanvir, N. R., Levan, A. J., González-Fernández, C., et al. 2017, ApJL, 848, L27
Totani, T. 2003, ApJ, 598, 1151
Troja, E., Castro-Tirado, A. J., Becerra González, J., et al. 2019, MNRAS, 489, 2104
Troja, E., Lipunov, V. M., Mundell, C. G., et al. 2017a, Natur, 547, 425
Troja, E., Piro, L., Ryan, G., van Eerten, H., & Zhang, B. 2020a, GCN, 27411, 1
Troja, E., Piro, L., van Eerten, H., et al. 2017b, Natur, 551, 71
Troja, E., van Eerten, H., Zhang, B., et al. 2020b, MNRAS, 498, 5643
Valenti, S., Benetti, S., Cappellaro, E., et al. 2008, MNRAS, 383, 1485
van Marle, A. J., Langer, N., Achterberg, A., & García-Segura, G. 2006, A&A, 460, 105
Vieira, N., Ruan, J. J., Haggard, D., et al. 2020, ApJ, 895, 96
Wanajo, S., Sekiguchi, Y., Nishimura, N., et al. 2014, ApJL, 789, L39
Watson, A. M., Butler, N. R., Lee, W. H., et al. 2020, MNRAS, 492 5916
Weinberg, S. 1972, Gravitation and Cosmology: Principles and Applications of the General Theory of Relativity (New York: Wiley)
Wijers, R. A. M. J., Rees, M. J., & Meszaros, P. 1997, MNRAS, 288, L51
Woosley, S., & Janka, T. 2005, NatPh, 1, 147
Woosley, S. E. 1993, ApJ, 405, 273
Woosley, S. E., & Bloom, J. S. 2006, ARA&A, 44, 507
Yamazaki, R., Toma, K., Ioka, K., & Nakamura, T. 2006, MNRAS, 369, 311
Yang, B., Jin, Z.-P., Li, X., et al. 2015, NatCo, 6, 7323
Yi, S.-X., Wu, X.-F., & Dai, Z.-G. 2013, ApJ, 776, 120
Zhang, B., & Mészáros, P. 2001, ApJ, 559, 110